



**HAL**  
open science

## New Cloud System Metrics to Assess Bulk Ice Cloud Schemes in a GCM

Claudia Stubenrauch, Marine Bonazzola, Sofia E Protopapadaki, Ionela Musat

► **To cite this version:**

Claudia Stubenrauch, Marine Bonazzola, Sofia E Protopapadaki, Ionela Musat. New Cloud System Metrics to Assess Bulk Ice Cloud Schemes in a GCM. *Journal of Advances in Modeling Earth Systems*, 2019, 10.1029/2019MS001642 . hal-02344619

**HAL Id: hal-02344619**

**<https://hal.sorbonne-universite.fr/hal-02344619v1>**

Submitted on 4 Nov 2019

**HAL** is a multi-disciplinary open access archive for the deposit and dissemination of scientific research documents, whether they are published or not. The documents may come from teaching and research institutions in France or abroad, or from public or private research centers.


L'archive ouverte pluridisciplinaire **HAL**, est destinée au dépôt et à la diffusion de documents scientifiques de niveau recherche, publiés ou non, émanant des établissements d'enseignement et de recherche français ou étrangers, des laboratoires publics ou privés.



## RESEARCH ARTICLE

10.1029/2019MS001642

## New Cloud System Metrics to Assess Bulk Ice Cloud Schemes in a GCM

Claudia J. Stubenrauch<sup>1</sup> , Marine Bonazzola<sup>1</sup>, Sofia E. Protopapadaki<sup>1,2</sup>, and Ionela Musat<sup>1</sup><sup>1</sup>Laboratoire de Météorologie Dynamique/Institut Pierre-Simon Laplace, Sorbonne Université, Ecole Polytechnique, CNRS, Paris, France, <sup>2</sup>COOPETIC, Paris, France

## Key Points:

- Cloud System Metrics for process-oriented diagnostics
- Bulk ice cloud scheme for climate models
- IR Sounder cloud observation simulator

## Supporting Information:

- Supporting Information S1

## Correspondence to:

C. J. Stubenrauch,  
stubenrauch@lmd.polytechnique.fr

## Citation:

Stubenrauch, C. J., Bonazzola, M., Protopapadaki, S. E., & Musat, I. (2019). New cloud system metrics to assess bulk ice cloud schemes in a GCM. *Journal of Advances in Modeling Earth Systems*, 11. <https://doi.org/10.1029/2019MS001642>

Received 29 JAN 2019

Accepted 31 AUG 2019

Accepted article online 6 SEP 2019

**Abstract** Bulk microphysical properties of ice clouds, such as fall speed and ice crystal size distribution, strongly impact the life time and the radiative effects of these clouds. Three coherent bulk ice schemes, with fall speed and effective ice crystal diameter depending on both ice water content and temperature, have been constructed from published parameterizations. We present a novel upper tropospheric cloud system concept to study the impact of these schemes on the LMDZ climate simulations. For this evaluation, cloud data from hyperspectral infrared sounders Atmospheric InfraRed Sounder and IR Atmospheric Sounding Interferometer are used, because they include cirrus with visible optical depths as low as 0.2. The analogous satellite observation simulator, developed for this purpose, is also presented. The cloud system concept, applied to the data and to the simulator outputs, allows a process-oriented evaluation. In general, the new bulk ice schemes lead to a better agreement with the cloud data, in particular concerning the cloud system property distributions and the relation between cloud system properties and proxies mimicking the life stage and the convective depth. Sensitivity studies have demonstrated that both the introduction of the new schemes as well as the necessary adjustment of the relative width of the upper tropospheric subgrid water distribution lead to these improvements. Our studies also suggest to revise the formulation of the latter.

**Plain Language Summary** Bulk microphysical properties of ice clouds, such as fall speed and ice crystal size distribution, strongly impact the life time and the radiative effects of these clouds. Both have to be predicted from other variables in a climate model. Three bulk ice schemes, depending on both ice water content and temperature, have been constructed from existing parameterizations, based on a large statistics of observations. The impact of these new schemes, when integrated into the LMDZ climate model, is studied. For the evaluation with cloud data from infrared sounders, a specific satellite observation simulator was developed which makes the simulation results look like the observed cloud layers. A novel cloud system concept, applied on the data and on the simulator results, allows a process-oriented evaluation and demonstrates improvements linked to the introduction of the new schemes themselves, but also to the necessary adjustment of another parameter which is linked to the subgrid variability of the upper tropospheric water.

## 1. Introduction

Upper tropospheric (UT) clouds, covering about 30% of the Earth (e.g., Stubenrauch et al., 2013), play a crucial role in the climate system by modulating the Earth's energy budget and heat transport. UT ice clouds (cirrus) either emerge as the outflow of convective and frontal systems, or form in situ in cold air supersaturated with water. Both their evolution with climate change and their feedback can only be reliably estimated if these cloud systems are adequately represented in general circulation models (GCM), the atmospheric component of Earth system models. At a spatial resolution of about 100 km, GCMs characterize the global atmospheric circulation. However, key processes at smaller scales, in particular convection and microphysics, have to be parameterized. Due to differences in these parameterizations, the intermodel spread of UT cloud properties is still large (IPCC; Boucher et al., 2013). Total shortwave and longwave feedback of high clouds, simulated by the models participating in phase 2 of the Cloud Feedback Model Intercomparison Project, vary within 1 Wm<sup>2</sup>/K, respectively (Zelinka et al., 2016).

Unconstrained parameters, mostly related to clouds and convection, are in general “tuned” (Hourdin et al., 2017), so that the simulated present-day climate system is close to radiative balance at the top of the atmosphere (TOA) and matches global observations (i.e., surface temperatures and cloud amount). Some of

©2019. The Authors.

This is an open access article under the terms of the Creative Commons Attribution-NonCommercial-NoDerivs License, which permits use and distribution in any medium, provided the original work is properly cited, the use is non-commercial and no modifications or adaptations are made.

these parameters, such as mass-weighted or bulk ice crystal fall speed,  $v_m$ , or the balance between precipitating water and condensate available for detrainment, strongly influence the occurrence and properties of UT clouds and even climate sensitivity (e. g. Sanderson et al., 2008).

In a coherent bulk ice cloud scheme, the effective ice crystal diameter,  $D_{\text{eff}}$ , which influences cloud radiative effects, and  $v_m$ , linked to cloud physics, should follow observational relationships (e.g., Heymsfield, 2003; Mitchell et al., 2011; hereafter H03 and M11). These two parameters are closely related, because they both depend on the ratio of ice crystal mass over ice crystal area. Introducing this  $v_m$ - $D_{\text{eff}}$  dependence into the LMDZ GCM then removes the ability to tune  $v_m$ , as is currently done (Hourdin et al., 2013), with a scaling factor of 0.3.

In this article we present original observational metrics for a process-oriented assessment of parameterizations influencing UT clouds, such as a bulk ice cloud scheme. To improve the current  $v_m$  and  $D_{\text{eff}}$  parameterizations in the LMDZ GCM, we have constructed more coherent bulk ice cloud schemes from published parameterizations, deduced from large statistics of recent airborne and ground-based observations, by paying attention to their validity range. In these schemes  $v_m$  has realistic values compared to observations, in contrast to the tuned, much smaller  $v_m$  values of the current LMDZ GCM version. The integration of these bulk ice schemes into the model then demanded a scaling adaptation of the remaining unconstrained parameters sensitive to UT clouds, so that TOA radiation balance is guaranteed.

It is a challenge to build a parameterization of realistic bulk ice crystal fall speed at the spatial resolution of a GCM, because size and habit of the ice crystals are largely variable and depend on many factors, among them the formation process and the life stage of the cloud as well as the atmospheric environment. On the other hand, airborne field campaigns and ground-based stations have collected numerous measurements within ice clouds, which provide valuable insight into the behavior of their microphysical properties. Despite the large variability, Field et al. (2007, hereafter F07) have shown that IWC and T are able to classify the distributions of ice crystal size and habit. Those GCMs that do not include a detailed microphysical scheme simulating ice crystal formation, which is often based on many assumptions, use a bulk ice cloud scheme. The latter may express  $v_m$  and  $D_{\text{eff}}$  or the ice crystal size distribution (PSD) itself as function of IWC and T (e.g., H03; Deng & Mace, 2008, hereafter DM08; F07; Furtado et al., 2015, hereafter F15).

For the evaluation of the UT cloud properties predicted by the LMDZ GCM, we use satellite retrievals from the Atmospheric InfraRed Sounder (AIRS) and the IR Atmospheric Sounding Interferometer (IASI) measurements (Stubenrauch et al., 2017). These instruments are sensitive to cirrus down to an IR emissivity,  $\epsilon_{\text{cid}}$ , of 0.1, during daytime and nighttime. To perform a consistent comparison between the simulation results and the data, a specific satellite observation simulator was built and integrated into the LMDZ model.

For a more process-oriented evaluation, we use a novel cloud system concept (Protopapadaki et al., 2017), which allows to relate the anvil properties to those of the convective cores. While classic cloud system approaches are based on the infrared (IR) brightness temperature and therefore only consider the thicker anvil parts (e.g., Liu et al., 2007; Machado et al., 1998; Roca et al., 2014; Yuan & Houze, 2010), this new concept uses two separate variables to construct the cloud systems: pressure (or height),  $p_{\text{cid}}$ , and emissivity,  $\epsilon_{\text{cid}}$ . The latter allows to distinguish between convective core, cirrus anvil, and thin cirrus within these systems. By mimicking the maturity stage of the convective systems via convective core fraction within the systems (decreasing from early development to dissipation), as already introduced by Machado et al. (1998), and by using the minimum temperature of the convective cores of mature convective systems as a proxy of convective depth, these new observational metrics provide additional constraints for parameterizations which influence the occurrence and properties of UT clouds.

In section 2 we discuss issues to be taken into account for a parameterization of  $v_m$  and  $D_{\text{eff}}$  in a GCM, and we present a synthesis of existing parameterizations, from which we deduce strategies for bulk ice cloud schemes to be tested in the LMDZ GCM. Section 3 describes the LMDZ model, together with the data and methods used for the evaluation. Sections 4 and 5 present (1) the assessment of the radiatively balanced simulations using the different bulk ice schemes and (2) the sensitivity studies concerning the most relevant tuning parameters for representing the UT cloud properties. While section 4 compares statistics of atmospheric and UT cloud system properties, section 5 presents the new observational process-oriented diagnostics by making full use of the novel cloud system concept. Conclusions and an outlook are given in section 6.

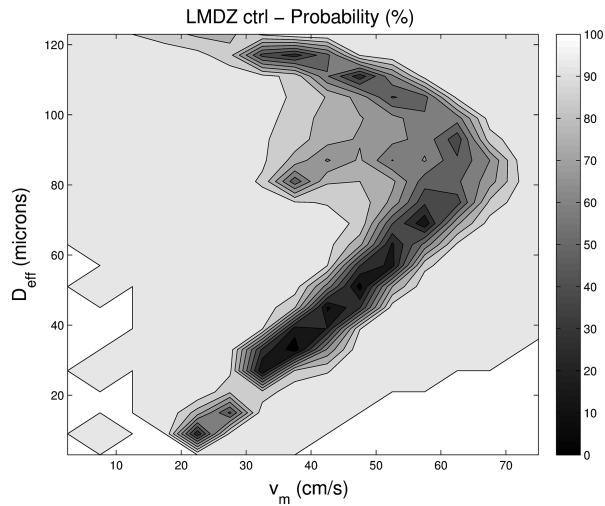


**Figure 1.** Ice cloud probability distribution (%) in the current version of the LMDZ GCM in the  $v_m/D_{\text{eff}}$  space.

The analytical expressions to derive bulk ice properties from the ice crystal diameter,  $D$ , as well as all parameterizations used in this article are given in the supporting information.

## 2. Synthesis of Existing Parameterizations and Strategy for Coherent Bulk Ice Cloud Schemes

### 2.1. Motivation

The current version of the LMDZ model utilizes a parameterization of  $v_m$  which depends on IWC (Heymsfield & Donner, 1990, hereafter HD90), while  $D_{\text{eff}}$  increases linearly with  $T$  between  $-84.1$  °C and  $0$  °C (Suzuki et al., 1993). In this way,  $v_m$  and  $D_{\text{eff}}$  are only loosely related, leading to the ice cloud probability distribution in the  $v_m$ - $D_{\text{eff}}$  space presented in Figure 1. This figure exhibits a  $v_m$  increasing with  $D_{\text{eff}}$  for  $D_{\text{eff}} < 70$   $\mu\text{m}$ , as expected, but for the largest  $D_{\text{eff}} (>100$   $\mu\text{m})$   $v_m$  is relatively small ( $<50$  cm/s). This latter behavior is not in agreement with the observations (e.g., H03, M11) and theory, as both  $D_{\text{eff}}$  and  $v_m$  are closely related to the ratio of ice crystal mass,  $m$ , over ice crystal area,  $A$ .

The bulk ice properties  $v_m$  and  $D_{\text{eff}}$  are determined by integration over the PSD or from the moments of the PSD. More details are given in equations S1–S23 in the supporting information. Recently, F07 have shown that one needs both, IWC and  $T$ , to classify the PSDs. The classification as function of  $T$  makes sense not only because of changing crystal habit but also because of a broadening of the PSD, with a relatively larger contribution of larger particles with increasing  $T$  (e.g., Heymsfield et al., 2013).

Our goal is to build a coherent  $v_m$ - $D_{\text{eff}}$  scheme, so that the radiative properties of cirrus are linked to realistic fall speeds. Linking  $v_m$  and  $D_{\text{eff}}$  removes the ability to tune  $v_m$ . We introduce a new bulk ice scheme with

1. a  $v_m$  parameterization which depends on both IWC and  $T$ , based on published parameterizations obtained from large statistics of recent observations, and which is valid over the whole  $T$  and IWC range in a GCM,
2. a  $D_{\text{eff}}$  parameterization which also depends on both IWC and  $T$  or which directly depends on  $v_m$ , again based on published parameterizations.

In the following we synthesize existing  $v_m$  parameterizations and relationships between  $v_m$  and  $D_{\text{eff}}$  obtained from recent airborne and ground-based observations, from which we then deduce new ice cloud schemes, by paying particular attention to the representativeness and validity range of the parameterizations.

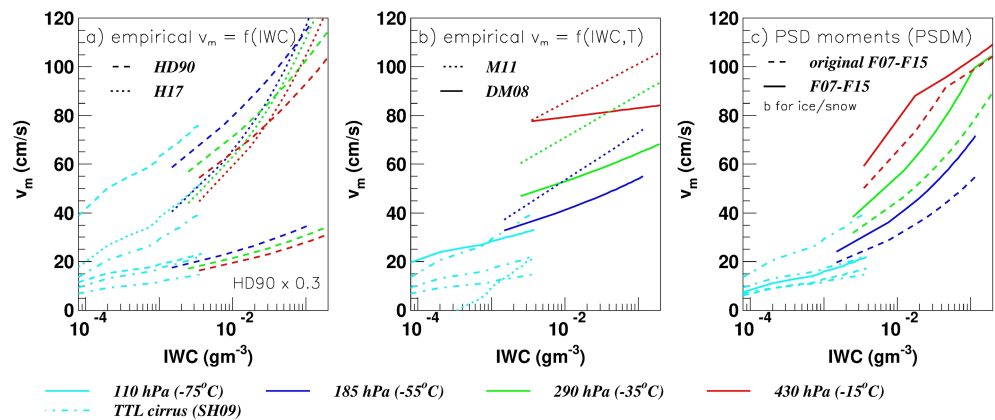
### 2.2. $v_m$ Parameterizations

Figure 2 compares the  $v_m$  parameterization of the current LMDZ model version to those obtained by analyzing recent observations, as a function of IWC for different  $T$ . For illustration we consider a tropical atmosphere, for which a specific  $T$  corresponds to a specific pressure,  $p$ . The analytical expressions of these parameterizations are summarized in equations S10–S31.

The  $v_m$  parameterization of the current LMDZ model version depends on the IWC only, based on observational evidence for gravitational sedimentation of ice crystals (HD90). Furthermore, the simulations for the Coupled Model Intercomparison Project phase 6 (Eyring et al., 2016) were performed using a  $v_m$  scaling factor of 0.3, for achieving radiative balance at TOA.

Figure 2a compares the empirical  $v_m$  parameterization of HD90, without and with scaling factor, with a more recent empirical parameterization developed by Heymsfield et al., 2017 (H17). Both parameterizations are expressed as a function of IWC only, but a small dependence on  $T$  comes from pressure corrections. H17 used measurements from 11 aircraft field programs, spanning latitudes from the Arctic to the tropics and  $T > -86$  °C and  $\text{IWC} > 10^{-3}$   $\text{gm}^3$ . Both parameterizations show a strong  $v_m$  increase with IWC. The newer one has a steeper slope, as also measurements of TTL cirrus were included, while the first parameterization was developed from cirrus measurements during three field campaigns with  $T > -60$  °C.





**Figure 2.** Bulk fall speed  $v_m$  parameterizations as function of IWC in a typical tropical atmosphere, at four different pressures (T): (a) HD90 and H17, (b) DM08 and M11, and (c)  $v_m$  from PSD moment parameterization of F07 and F15, once the original parameterization assuming ice crystal aggregates and once two different habits for ice and snow in the mass-diameter relation. In addition,  $v_m = f(IWC)$  of SH09 for cold TTL cirrus is indicated on each figure, with upper limit, median, and lower limit. The equations of all parameterizations are given in equations S10–S23.

Schmitt & Heymsfield (2009, hereafter SH09) developed a  $v_m$  parameterization specifically for nonconvective cold TTL cirrus, covering T between  $-86^\circ\text{C}$  and  $-56^\circ\text{C}$  and IWC between  $0.0001$  and  $0.003\text{ gm}^{-3}$ , using measurements of two field campaigns. This empirical  $v_m$  parameterization, which depends on IWC only, is also shown in Figure 2, as median (equation S10), lower limit (equation S11), and upper limit (equation S12). As expected,  $v_m$  for cold TTL cirrus is quite small (below  $20\text{ cm/s}$ ). The  $v_m$  parameterization of H17, which used a small fraction of TTL cirrus, lies slightly above the upper limit of the SH09 parameterization for T at  $-75^\circ\text{C}$  (corresponding to  $110\text{ hPa}$ ), while the  $v_m$  parameterization of HD90, which used only warmer cirrus, lies much above. It is interesting to note that the current LMDZ  $v_m$  scaled by  $0.3$  coincides well with the SH09 parameterization for  $\text{IWC} < 0.001\text{ gm}^{-3}$ , but has much smaller values than those observed for larger IWC, the latter range corresponding to the majority of ice clouds (Delanoë et al., 2011).

Figure 2b presents two empirical  $v_m$  parameterizations which directly depend on IWC and on T (DM08, M11). The motivation for such a parameterization was that critical ice cloud processes may depend also on large-scale dynamics and that both, IWC and T, are (or can be derived from) prognostic variables in climate models. However, the statistics within the IWC-T space is not evenly distributed: often at cold T only small IWC values exist, while large IWC is mostly found at warm T (e.g., DM08, Figure 2). This dependence is generally explained by water availability according to the Clausius-Clapeyron relationship, and may lead to a biased validity: the parameterized  $v_m$  for small IWC may be more reliable for small T than for large T and  $v_m$  for large IWC may be more reliable for large T than for small T.

The statistics for the DM08 parameterization is the largest available: about 30,000 hr of cirrus observations between 1999 and 2005, collected from ground-based millimeter cloud radar measurements at two ARM Climate Research Facilities, one in the tropics (Tropical Western Pacific) and one in the midlatitudes (Southern Great Plains). For the retrieval of  $v_m$  a conceptual model was developed which describes the radar reflectivity, Doppler velocity, and Doppler spectrum width by convoluting a  $\Gamma$ -like distribution of ice crystals with a turbulent spectrum undergoing mean vertical motion (Deng & Mace, 2006). In comparison with airborne measurements, Deng and Mace (2006) estimated instantaneous uncertainties of retrieved  $v_m$  to about  $20\text{ cm/s}$ . The consistency between the remote and in situ data is important as it illustrates that the retrieval method can be used to develop valid parameterizations even though radar is mostly sensitive to large particles. This ground-based statistics is much larger than the one of the airborne measurements, but does not include laminar cirrus found in the TTL. The analysis suggested that relationships are similar for tropical anvil cirrus and midlatitude synoptic cirrus, and therefore, we only present the  $v_m$  parameterization which was fitted over the entire statistics.

M11 analyzed PSD measurements with reduced shattered ice particles from three recent field campaigns in the tropics and Arctic. Again, TTL cirrus were not included. Relationships of  $v_m$  as function of IWC and T

were studied separately for in situ cirrus, anvil cirrus, aged anvil cirrus, and Arctic cirrus. A fit over the first three types of cirrus suggests an increase of  $v_m$  with IWC and T, with data points for T between  $-70$  °C and  $-20$  °C and IWC between  $0.00002$  and  $0.9$   $\text{gm}^3$ , while for Arctic cirrus a dependence on IWC was not detectable for a relatively warm T, ranging between  $-37$  °C and  $-21$  °C.

Both parameterizations compare relatively well in an IWC range between  $0.001$  and  $0.01$   $\text{gm}^3$ , and both increase with IWC and T. However, Figure 2b also reveals differences in the behavior with IWC and T: the M11 parameterization presents a stronger increase of  $v_m$  with increasing IWC, and the slope stays almost unchanged with T. The DM08 parameterization shows a much more restricted range of  $v_m$  (20 to 80 cm/s) and a decrease in slope with increasing T. Indeed, it does not only take into account independent terms of T and IWC but also terms combining T and IWC (equation S15). Although a very large statistics was used, by considering carefully the observations and the fits in Figure 2 of DM08, the parameterized  $v_m$  does not reach the highest observed values of  $v_m$  at large IWC which are around 100 cm/s. Compared to the SH09 parameterization for TTL cirrus, the  $v_m$  at  $-75$  °C of DM08 agrees relatively well with the upper limit of SH09, while the  $v_m$  parameterization of M11 would already reach 0 at  $0.0005$   $\text{gm}^3$ .

Figure 2c finally presents  $v_m$  based on the parameterization of the ice crystal PSD itself. F07 developed a parameterization of the PSD moments as a function of T, assuming a predominant ice crystal habit of aggregates. This PSD moment parameterization of F07 assumes an average T dependence, without distinguishing cirrus types and therefore formation processes, but it introduces differences by linking all moments of the PSD to the IWC (equations S17–S23). A relatively large sample of 13,000 PSDs, measured during four airborne field campaigns (two in the tropics and two in the midlatitudes, with  $T > -60$  °C), has been analyzed to guarantee a good sampling.

The bulk fall speed  $v_m$ , which is determined from the terminal fall velocity  $v_t$  of a single ice or snow crystal by integration over the PSD, is then a function of T and IWC. The terminal fall velocity  $v_t$  is often expressed as a power law of the ice crystal diameter D:  $v_t = eD^f$ , with  $e$  and  $f$  determined for specific ice crystal habits (e.g., Ferrier, 1994; Mitchell, 1996). F15 conclude that two couples ( $e, f$ ) are needed in their climate simulations to reproduce observed IWCs, with ( $e, f$ ) = (1,042, 1.0) for ice and ( $e, f$ ) = (14.3, 0.416) for snow (in SI units). Choosing for each D the smallest  $v_t$  of both coincides with ice for  $D < 600$   $\mu\text{m}$  and snow for  $D > 600$   $\mu\text{m}$ . Figure 2c presents this  $v_m$  parameterization based on F15 and F07, once supposing ice crystal aggregates and once using different habits for ice and snow. Again,  $v_m$  increases both with IWC and with T, covering a range between 5 and 110 cm/s. The slope with IWC is larger than the ones of M11 and DM08, except at  $-75$  °C, where this parameterization agrees remarkably well with the one for TTL cirrus of SH09, although TTL cirrus were not included in the data to develop the PSD moment parameterization. Furthermore, the slope decreases at large IWC and large T. Compared to the parameterizations of Heymsfield in Figure 2a, the values agree with the ones at larger T, while for colder cirrus the  $v_m$  values of Heymsfield seem to be overestimated.

To summarize, compared to the  $v_m$  parameterizations of Heymsfield which only depend on IWC (Figure 2a), the introduction of the additional T dependence leads to a smaller slope of  $v_m$  with IWC for a specific T. In addition, it allows the  $v_m$  of cirrus with the same IWC to differ according to T-dependent changes in ice crystal sizes and habits, leading to a larger  $v_m$  at larger T. As in general IWC increases with T, this partly explains the steeper slope of  $v_m$  with IWC for the parameterizations of Figure 2a. However, the  $v_m$  values at large IWC are even larger than for the other parameterizations at large IWC and large T. This can be probably explained by the fact that it is difficult to find a function depending only on IWC to correctly fit the data.

In the following we will consider the parameterizations of F07–F15 and of DM08, the latter extended toward cold T by SH09. Both were built from large observational statistics, but different approaches and data types have led to a different behavior of the parameterizations. Therefore, we will test their impact in the LMDZ simulations.

### 2.3. Relationship Between $v_m$ and $D_{\text{eff}}$

Field campaigns found robust relationships between  $D_{\text{eff}}$  and  $v_m$ , as these both depend on  $m/A$ . While H03 fitted this relationship separately for anvil cirrus and for synoptic cirrus, M11 developed fits separately for the tropics and for the Arctic. The range of these parameterizations is shown in Figure 3. In this way, a larger  $D_{\text{eff}}$

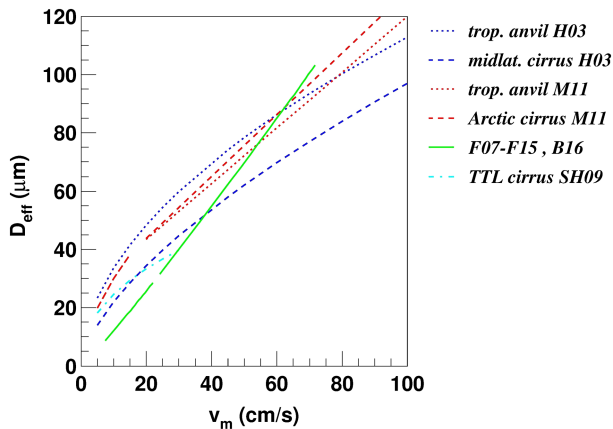


**Figure 3.** Relationships between generalized effective ice crystal diameter  $D_{\text{eff}}$ , defined by equation S9, and bulk fall speed  $v_m$ . Empirical parameterizations by H03, M11, and SH09 compared to results obtained from the PSD moment parameterization (F07 and F15) and  $D_{\text{eff}}$  determined from B16. The equations of all parameterizations are given in equations S24–S31.

corresponds to a larger  $v_m$ , as expected, with  $D_{\text{eff}}$  of about  $20 \mu\text{m}$ , for  $v_m$  around  $5 \text{ cm/s}$ , and  $D_{\text{eff}}$  in a range between  $80$  and  $105 \mu\text{m}$ , for  $v_m$  around  $80 \text{ cm/s}$ . The range is given by sampling tropical, midlatitude synoptic, and Arctic cirrus. While H03 and M11 agree quite well for tropical cirrus, midlatitude synoptic cirrus seem to have a larger fall speed than Arctic cirrus for similar  $D_{\text{eff}}$ , which indicates that the ice crystals of midlatitude cirrus might have a larger density. On the other hand, all curves coincide at the lower end with the one for thin TTL cirrus of SH09.

We also investigate relationships between  $v_m$  and  $D_{\text{eff}}$ , both being determined from the same PSDs, using parameterizations of F07, F15, and Baran et al., 2016 (B16). However, instead of parameterizing  $D_{\text{eff}}$ , Baran et al. (2014) and B16 directly parameterized the bulk ice spectral optical properties as a function of IWC and T, by averaging over the PSDs measured and parameterized by F07. Therefore, Baran and Labonnote (2007) developed an ensemble model of ice crystals, built of six different ice crystal habits within the PSD. With increasing crystal size the proportion of hexagonal columns decreases while the proportion of aggregates increases, leading to different weights of each member of the ensemble model at each size interval of the PSD. Such a parameterization is attractive,

as the definition of  $D_{\text{eff}}$  is not generally applicable across the whole electromagnetic spectrum (e.g., Baran, 2012). However, the parameterization of B16 cannot directly be implemented into the LMDZ GCM, as the spectral bands are not the same as the ones used for the radiative transfer of the LMDZ (see sections 3.1 and 6).

Nevertheless, for illustration, Figure 3 of B16 presents the bulk single scattering albedo,  $\omega_0$ , at  $1.6 \mu\text{m}$  (a) as a function of  $D_{\text{eff}}$  (computed from the first member of the ensemble model, the hexagonal ice column of aspect ratio 1) and (b) as a function of the ratio between the third and second moment,  $M_3/M_2$ , corresponding to  $D_m$  assuming the same model. B16 deduce from this figure that  $D_{\text{eff}}$  and  $D_m$  are proportional, and we have computed the factor of conversion from Figures 3a and 3b approximately as  $0.17$ , so that  $D_{\text{eff}} \cong 0.17 D_m$ , with  $D_m$  obtained from the PSDM parameterization of F07. This relatively crude estimation will be just used to compare the impact of (1) a parameterization which directly derives  $D_{\text{eff}}$  from  $v_m$ , but using a different data source than the  $v_m$  parameterization, and (2) the PSDM parameterizations of  $v_m$  and  $D_{\text{eff}}$ , using the same PSDs but a rough estimation of  $D_{\text{eff}}$ .

Figure 3 compares the relationship between  $D_{\text{eff}}$  and  $v_m$  of the PSDM parameterization of F07–F15 and B16 to the empirical  $D_{\text{eff}}/v_m$  parameterizations of H03, M11, and SH09. The relationship between  $D_{\text{eff}}$  and  $v_m$ , obtained from F07–F15 and B16, is mostly linear, while  $D_{\text{eff}}$  evolves more slowly with  $v_m$  toward larger  $v_m$  according to the empirical parameterizations of H03, M11, and SH09 (equations S25–S32). This difference in behavior may be linked to changing crystal habits. Nevertheless, for  $40 \text{ cm/s} < v_m < 90 \text{ cm/s}$  the  $D_{\text{eff}}$  of the PSD moment parameterization lies within the range of the other observations, while  $D_{\text{eff}}$  lies below for smaller  $v_m$ .

From these parameterizations, derived from different airborne measurements, we conclude that

1. at large  $D_{\text{eff}}$ , the relationship in the current version of the LMDZ model, given in Figure 1, does not match the parameterizations obtained from observations in Figure 3;
2.  $D_{\text{eff}}$  can be estimated from  $v_m$  within an uncertainty of about  $\pm 5 \mu\text{m}$  (at smaller  $v_m$ ) to  $\pm 10 \mu\text{m}$  (at larger  $v_m$ ), leading to the possibility to estimate  $D_{\text{eff}}$  in the GCM directly from a  $v_m$  parameterization, which depends itself on IWC and T.

#### 2.4. Construction of Coherent Ice Cloud Schemes

We select from Figure 2 two parameterizations which predict  $v_m$  from IWC and T: the empirical parameterization of DM08 deduced from ground-based retrievals (Figure 2b) and the PSD moment parameterization of F07–F15 from airborne in situ measurements (Figure 2c). Both have been determined with large statistics. As the latter agrees quite well with the parameterization for TTL cirrus, we will employ this

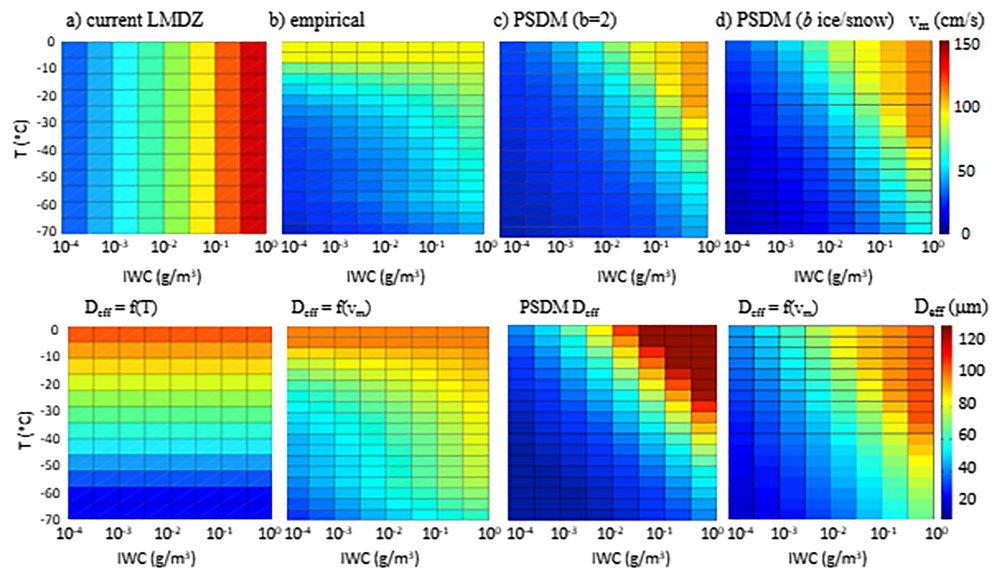


**Figure 4.** (top panel) Bulk fall speed  $v_m$  and (bottom panel) generalized effective ice crystal diameter  $D_{eff}$  as a function of IWC and  $T$  for the current LMDZ bulk ice scheme (a) and for the new bulk ice schemes described above: (b) empirical  $v_m$  and  $D_{eff}(v_m)$ , (c) PSDM  $v_m$  and  $D_{eff}$ , and (d) PSDM  $v_m$  and  $D_{eff}(v_m)$ .

parameterization over the whole  $T$  range, whereas the DM08 parameterization will be extended toward the SH09 parameterization for cold  $T$ .

To link  $D_{eff}$  to  $v_m$ , we use the mean relationship of the parameterizations by H03. For sensitivity studies we will also use  $v_m$  and  $D_{eff}$  from the PSD moment parameterizations (PSDM) of F07–F15 and B16 (section 2.3).

Thus, we will test the following bulk ice schemes in the LMDZ GCM:

1. *empirical  $v_m$  and  $D_{eff}(v_m)$* :  $v_m$  empirically parameterized as a function of IWC and  $T$  from multiannual ground-based retrievals of DM08, extended by the IWC-dependent  $v_m$  parameterization of SH09 for  $T < -60^{\circ}C$ , and  $D_{eff}$  as the mean of the  $D_{eff}$ - $v_m$  relationships for synoptic cirrus and anvil cirrus determined by H03 (Figure 4b). The scheme is implemented using equations S35–S37.
2. *PSDM  $v_m$  and  $D_{eff}$* :  $v_m$  and  $D_m$  from the PSD moment parameterizations of F07 and F15, assuming aggregated crystals for the  $m$ - $D$  relationship ( $b = 2$ ), with  $D_{eff} \cong 0.17 D_m$ , roughly adapted from B16. These parameterizations are based on the same measured PSDs (Figure 4c). The scheme is implemented using equations S38–S44.
3. *PSDM  $v_m$  and  $D_{eff}(v_m)$* :  $v_m$  from the PSD moment parameterizations of F07–F15, using both (a, b) and (e, f) separately for ice and snow (see supporting information).  $D_{eff}$  is predicted from  $v_m$  again as the mean of the  $D_{eff}$ - $v_m$  relationships for synoptic cirrus and anvil cirrus determined by H03 (Figure 4d). The scheme is implemented using equations S45–S51.

Figure 4 illustrates the behavior of  $v_m$  (top panel) and of  $D_{eff}$  (bottom panel) in the IWC/ $T$  space for these different bulk ice schemes, compared to the one of the current LMDZ version (Figure 4a). The fully empirical parameterization (Figure 4b) suggests a smaller range of  $v_m$  and  $D_{eff}$  and a weaker increase of  $v_m$  and  $D_{eff}$  with IWC and  $T$ , than the PSDM schemes (Figures 4c and 4d). Largest differences occur at warm  $T$  and large IWC (i.e., in the top right domain of the IWC/ $T$  space), which is infrequently occupied by UT clouds: the PSDM schemes predict larger  $v_m$  and larger  $D_{eff}$  than the empirical scheme. In the range of largest probabilities in the IWC/ $T$  space for UT ice clouds (i.e.,  $-70^{\circ}C < T < -10^{\circ}C$  and  $10^{-3.5} < IWC < 10^{-1} gm^3$ ), which corresponds to more than 50% of UT cloud occurrences in the LMDZ GCM (Figure 6), the empirical scheme predicts slightly larger  $v_m$  and larger  $D_{eff}$  than the PSDM schemes. The two PSDM parameterizations provide a similar behavior of  $v_m$ , while a slightly reduced range in  $D_{eff}$  is found when the empirical  $D_{eff}$ - $v_m$  relationship of H03 is used (Figures 4c and 4d). Larger ice crystals in general reflect less and absorb more radiation, so this should have an impact on the radiative effect of the ice clouds.



### 3. Model, Data, and Methods

In this section we briefly describe the LMDZ GCM (section 3.1), as well as the AIRS and IASI cloud data (section 3.2) used to assess the properties of the simulated UT cloud properties. For a consistent comparison with these data, the model outputs first need to be processed by a specific cloud observation simulator (section 3.3) that filters the simulated clouds with the IR sounder detection sensitivity and builds the cloud properties in such a way that they correspond to the retrieved ones (observed from above). The methodology to construct the UT cloud systems, to be applied both on the observations and the simulations at the same spatial resolution, is described in section 3.4.

#### 3.1. LMDZ Model Configuration

The LMDZ GCM (Hourdin et al., 2013) is the atmospheric component of the IPSL Earth system model. UT clouds are mostly formed by a large-scale condensation parameterization: the fractional cloudiness,  $c_{cld}$ , and condensed water,  $q_c$ , are defined as a function of a subgrid-scale distribution  $P(q)$  of total water  $q$  as

$$c_{cld} = \int_{q_{sat}}^{\infty} P(q) dq \quad (1)$$

$$q_c = \int_{q_{sat}}^{\infty} (q - q_{sat}) P(q) dq \quad (2)$$

where  $q_{sat}(T)$  is the saturation specific humidity averaged over the grid cell.

$P(q)$  is a generalized lognormal distribution, bounded at 0. The relative width of  $P(q)$  within the grid cell,  $\zeta(p) = \sigma/q$ , with  $\sigma$  being the standard deviation, is prescribed as a function of pressure:  $\zeta(p)$  increases linearly from 0 at surface to 0.002 at 500 hPa, then to RQH = 0.4 at 250 hPa.  $\zeta(p)$  is kept constant to RQH above, and RQH is one of the tuning parameters in the model.

A fraction  $q_{ice}$  of  $q_c$  is assumed to be frozen. This fraction varies as a function of  $T$ , from 0 at 273.15 K to 1 at 258.15 K. This means that all clouds at  $T < 258.15$  K only consist of ice crystals. The condensed water is partially precipitated. The frozen water  $q_{ice}$  satisfies the equation:

$$\frac{dq_{ice}}{dt} = \frac{1}{\rho} \frac{\partial}{\partial z} (FALLICE \rho q_{ice} v_m) \quad (3)$$

where FALLICE is a tuning factor and  $v_m$  is the bulk ice fall speed given as a function of IWC by HD90.

Convection is represented by a buoyancy sorting mass flux scheme (Emanuel, 1993), producing a population of convective towers within a grid cell, and assuming that ascent terminates at the level of neutral buoyancy. A recently developed parameterization (Rio et al., 2013) controls convection by subcloud lifting processes, including boundary layer thermals and evaporatively driven cold pools (Grandpeix & Lafore, 2010). The latter, particularly important over land, contribute to maintain deep convection and to initiate new convective cells.

For convective clouds, in contrast to large-scale or stratiform clouds, the standard deviation  $\sigma$  of  $P(q)$  is not prescribed, but computed as a function of the in-cloud condensed water,  $q_{cld} = q_c/c_{cld}$ , predicted by the convection scheme.

The model employs a relatively simple parameterization to partition between precipitation and detrained fraction of convective condensate, with the precipitation efficiency as a function of  $q_{cld}$  and  $T$  (Emanuel & Živković-Rothman, 1999). Precipitation efficiency is bounded by a maximum value, EPMAX, another tuning factor, which is slightly less than unity, to allow some cloud water to remain in suspension in the atmosphere instead of being entirely rained out (Bony & Emanuel, 2001).

Radiative fluxes in the current LMDZ version are computed by using the recently implemented Rapid Radiative Transfer Model for GCM (Morcrette et al., 2008), which has 16 bands in the longwave and 14 bands in the shortwave. Ice optical properties are parameterized following Ebert and Curry (1992), representing the ice crystals by poly-dispersed randomly oriented hexagonal cylinders whose size can be characterized by the generalized effective diameter  $D_{eff}$ , as defined by Fu (1996) in equation S9.  $D_{eff}$  is set to a constant value for liquid water clouds, and decreases with decreasing  $T$  (from 120  $\mu\text{m}$  at  $T = 273.15$  K to 7  $\mu\text{m}$  at  $T = 258.15$  K)



for ice clouds (Heymsfield & Platt, 1984; Suzuki et al., 1993). For the calculation of the cloud optical thickness, the vertical overlap of cloud layers is assumed to be maximum-random (Bony & Emanuel, 2001).

### 3.2. AIRS and IASI Cloud Data

The AIRS (Chahine et al., 2006) aboard the National Aeronautics and Space Administration Earth Observation Satellite Aqua and the IASI (Hilton et al., 2012) aboard the European Organisation for the Exploitation of Meteorological Satellite (EUMETSAT) Meteorological Operation satellite MetOp-A provide measurements at 1:30 AM and 1:30 PM local time (LT) since 2002 and at 9:30 AM and 9:30 PM LT since 2007, respectively. The spatial resolution of these measurements at nadir is about 13.5 and 12.0 km, respectively.

The Clouds from IR Sounders (CIRS) cloud data (Stubenrauch et al., 2017), now being produced and distributed by the French data center AERIS, are very similar to the AIRS-LMD cloud data (Stubenrauch et al., 2010), distributed at the French data center ICARE and evaluated in the GEWEX cloud assessment (Stubenrauch et al., 2013).

The retrieval is based on a weighted  $\chi^2$  method (Stubenrauch et al., 1999) using eight channels along the 15- $\mu\text{m}$   $\text{CO}_2$  absorption band, with peak contributions at 235, 285, 375, 415, 565, 755, 855 hPa, and surface. It provides cloud pressure ( $p_{\text{cld}}$ ), cloud emissivity ( $\epsilon_{\text{cld}}$ ), and cloud temperature ( $T_{\text{cld}}$ ) and cloud height ( $z_{\text{cld}}$ ). Upper tropospheric or high-level clouds are defined as clouds with  $p_{\text{cld}} < 440$  hPa. One advantage compared to the CALIPSO-GOCCP simulator is that the CIRS UT cloud types are further distinguished with respect to  $\epsilon_{\text{cld}}$  as high opaque (Cb:  $\epsilon_{\text{cld}} \geq 0.98$ ), cirrus (Ci:  $0.98 < \epsilon_{\text{cld}} \leq 0.5$ ), and thin cirrus (thCi:  $0.5 < \epsilon_{\text{cld}} \leq 0.1$ ).

### 3.3. Cloud Properties From the AIRS/IASI Cloud Observation Simulator

To be comparable with AIRS and IASI cloud data, the LMDZ simulation output needs to be processed as in other observational simulator packages (Bodas-Salcedo et al., 2011). Here we follow a methodology previously developed by Stubenrauch et al. (1997) and Hendricks et al. (2010) for the comparison of GCM cloud properties to those retrieved from IR sounders that we adapt to the specificities of the LMDZ model and the AIRS/IASI data.

The method takes into account several systematic differences between the AIRS/IASI cloud data and the LMDZ simulation output:

1. the different temporal sampling: while the model calculates the cloud fields every 0.5 hr, the satellite measurements are only available at 1:30 AM and 1:30 PM local time (AIRS) and at 9:30 AM and 9:30 PM local time (IASI);
2. the lower spatial resolution of the LMDZ simulation results ( $1.25^\circ$  latitude  $\times$   $2.5^\circ$  longitude) and therefore partial cover of cloud layers;
3. the different view on the cloud fields: while LMDZ calculates three-dimensional cloud fields, and simulates multiple vertically overlaying clouds, AIRS and IASI provide a view from above, providing only information on the highest cloud layer in the case of multiple cloud layers.
4. the instrument sensitivity: the CIRS retrieval determines clouds with an IR optical depth larger than 0.1;
5. the interpretation of retrieved variables: CIRS-retrieved  $p_{\text{cld}}$ ,  $T_{\text{cld}}$ , and cloud height,  $z_{\text{cld}}$ , are not given at cloud top but at the middle between cloud top and apparent cloud base, the latter corresponding to the cloud level where the clouds gets opaque (IR optical depth of 1.5, corresponding to  $\epsilon_{\text{cld}}$  of 0.6).

To reconstruct from the LMDZ simulation outputs the cloudiness that would be observed by AIRS and IASI, we make several assumptions on the simulated cloud layers. We first assume a maximum overlap of the cloudiness of contiguous cloud layers, defined as cloud blocks, and random overlap between different cloud blocks, vertically separated by cloud-free layers (Figure 5a).

Within the uppermost cloud block we define subcolumns, each of them being characterized by a different vertical distribution of cloud layers. The sum of the horizontal areas of all subcolumns corresponds then to the area of the uppermost cloud block and is given by the area of the maximum cloud layer among all cloud layers within the uppermost cloud block. By construction, within a subcolumn cloud layers cover 0% or 100% of the total subcolumn area. We therefore have in a given subcolumn one or several sets of vertically contiguous cloudy layers of 100% fractional coverage that we define as “subcolumn cloud blocks.” For each of them we calculate the total IR optical depth  $\tau_{\text{cld}}$  as the sum of the IR optical

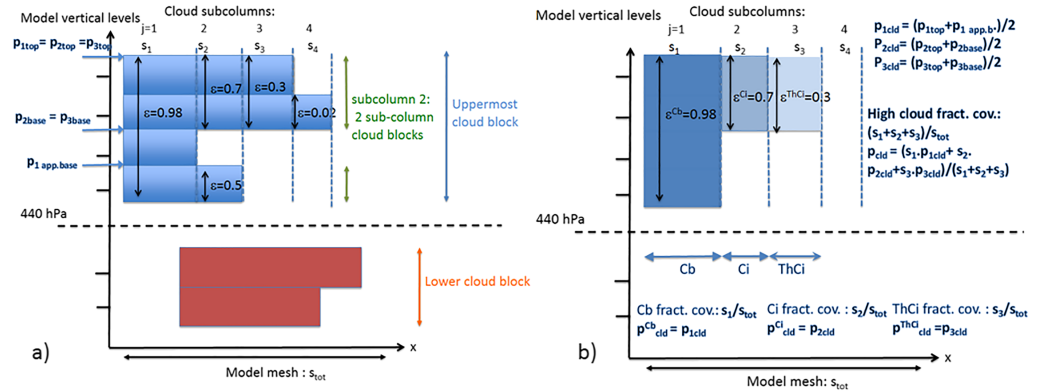


**Figure 5.** Schematic view of the CIRS simulator: (a) determination of cloud blocks and subcolumn cloud blocks and (b) determination of cloud-type properties.

depths given for each cloud layer and then transform  $\tau_{cld}$  into the IR emissivity  $\epsilon_{cld}$ . We neglect the subcolumn cloud blocks with  $\tau_{cld} < 0.1$ , since the CIRS retrieval only keeps clouds with  $\epsilon_{cld} > 0.1$  (corresponding to an IR optical depth  $\tau_{cld} > 0.1$ ). As the CIRS retrieval only determines the properties of the uppermost cloud, we neglect subcolumn cloud blocks that are located below the highest detected one. Thus, in each subcolumn (of index  $j$ ) we end up with no more than one detected subcolumn cloud block, characterized by its total emissivity  $\epsilon_j$ . This quantity then allows to determine the type of the subcolumn cloud block (i.e., Cb, Ci, or thCi; see section 3.2). The area of a given cloud type within the whole cloud block is obtained by summing the areas of the subcolumns which lie in the corresponding  $\epsilon$  range.

For a selected subcolumn cloud block  $j$ , we also calculate pressure  $p_j$  and temperature  $T_j$  at its top and its base. To compare  $p_{cld}$  with the one observed by AIRS and IASI, we also have to determine the cloud level at which the subcolumn cloud block yields an IR optical depth of 1.5. This level corresponds to the apparent cloud base. In the case of semitransparent clouds ( $\tau_{cld} < 1.5$  or  $\epsilon_{cld} < 0.6$ ),  $p_{cld} = 0.5 \times (p_{top} + p_{base})$ , while for more opaque clouds ( $\tau_{cld} > 1.5$ ),  $p_{cld} = 0.5 \times (p_{top} + p_{app\ base})$ , as has been shown in comparison with CALIPSO (Stubenrauch et al., 2010).

These variables,  $p_{cld}$ ,  $T_{cld}$ , and  $\epsilon_{cld}$  (noted as  $X$ ), are then determined over the whole uppermost cloud block by averaging the subcolumn variables ( $X_j$ ), weighted by the areas of the subcolumns (Figure 5b). They are also determined for each cloud type within the uppermost cloud block (noted as  $X^{Cb}$ ,  $X^{Ci}$ , and  $X^{thCi}$  or in general  $X^{cldtp}$ ) by averaging the subcolumn variables,  $X_j$ , weighted by the areas of the associated cloud types.

If within a model grid cell more than one cloud block occurs above the height of  $p_{cld} < 440$  hPa, the total cloud fractional coverage observed by the IR sounders from above can be calculated, according to random overlap, by

$$c_{tot} = 1 - \prod_k (1 - c_k) \quad (4)$$

where  $c_k$  is the fractional coverage of the cloud block  $k$ . We also calculate the fractional coverage of each high-level cloud type ( $cldtp$ ), by considering that it is the fractional coverage of the uppermost one, plus those located below and randomly masked by all cloud types that are located above:

$$c_{tot}^{cldtp} = c_1^{cldtp} + \sum_{k=2}^N \left[ c_k^{cldtp} \times \prod_{i=1}^{k-1} (1 - c_i) \right] \quad (5)$$

where  $N$  is the total number of cloud blocks ordered by decreasing cloud altitude and  $c_k^{cldtp}$  is the subcolumn contribution of cloud type  $cldtp$  to the individual fractional coverage of cloud block  $k$ .

Finally, the model grid cell variables for a given cloud type  $cldtp$  (noted as  $X_{tot}^{Cb}$ ,  $X_{tot}^{Ci}$ , and  $X_{tot}^{thCi}$  or in general  $X_{tot}^{cldtp}$ ) are derived by averaging over the values  $X_k^{cldtp}$  associated with the unmasked cloud blocks of this type:

$$X_{tot}^{cldtp} = c_1^{cldtp} X_1^{cldtp} + \sum_{k=2}^N \left[ c_k^{cldtp} X_k^{cldtp} \times \prod_{i=1}^{k-1} (1-c_i) \right] \quad (6)$$

### 3.4. Construction of UT Cloud Systems

For a more process-oriented evaluation, we construct cloud systems from UT clouds of adjacent grid cells and then study their horizontal extent and emissivity structure. This allows in particular to study convective cloud systems: Protopapadaki et al. (2017) have demonstrated that the evolution of convective cloud systems can be followed by using the convective core fraction within the cloud system as an indicator of life cycle stage (decreasing from formation toward dissipation). The study has also revealed that mature convective cloud systems include an increasing fraction of thin cirrus within/around their anvils as their temperature decreases (indicating an increasing convective depth). Although the spatial resolution of the LMDZ GCM (1.25° latitude × 2.5° longitude) is much coarser than the initial one of the cloud system data (0.5° latitude × 0.5° longitude), we will show that this approach still gives precious information for better constraining the parameterizations that influence the UT clouds.

On one hand we construct the UT cloud systems from the LMDZ model simulations, after having applied the cloud observation simulator, and on the other hand from the AIRS and IASI cloud data, gridded at GCM spatial resolution. We also consider the cloud-type statistics within the grid cells (Cb, cirrus, and thin cirrus). Compared to the initial observational study (Protopapadaki et al., 2017), we had to adapt the definition of convective cores in order to make consistent comparisons. As the control simulation revealed a much larger Cb fraction within the grid cells than the data gridded at the same spatial resolution (section 3 and Table 3), we identify the convective cores directly from the grid cell average  $\langle \epsilon_{cld} \rangle$ , with  $\langle \epsilon_{cld} \rangle \geq 0.95$ , instead of using a threshold on the Cb subgrid fraction. Due to the coarse spatial resolution, the threshold on the grid cell average had to be relaxed to this value, but in addition we require a Cb subgrid fraction  $> 0.1$  and precipitation within these identified “convective cores.” The rain rate within the convective cores of the cloud data is determined from Advanced Microwave Scanning Radiometer–Earth Observing System L2 precipitation data (Kummerow et al., 2015), which have been collocated with simultaneous AIRS cloud data. The spatial resolution of Advanced Microwave Scanning Radiometer–Earth Observing System data are about 5 km. These data have been used by Protopapadaki et al. (2017) to determine the  $\epsilon_{cld}$  threshold as 0.98 at 0.5° spatial resolution for the identification of the convective cores. We distinguish between UT cloud systems with no convective core (these might originate from dissipating convection or formed by in situ freezing) from those having single or multiple convective cores. In the case that a “convective core” just defined by  $\langle \epsilon_{cld} \rangle \geq 0.95$  and Cb subgrid fraction  $> 0.1$  includes no convective rain, the cloud system will be counted as a UT cloud system with no convective core.

For each cloud system we further compute its horizontal extent (size), the mean anvil emissivity, and the coldest temperature within the convective cores. To get an insight into the cloud system horizontal structure, we also compute the fraction of thin cirrus cover over total (thin and thick) cirrus cover, and for convective systems, the convective core fraction.

## 4. Climate Simulations and Their statistical Evaluation

### 4.1. Climate Simulation Experiments

The LMDZ model provides IWC, obtained from  $q_{ice}$ , and T at each pressure level. Both are used to compute  $v_m$  and  $D_{eff}$ , using equations S33 and S34 in the control simulation (CNTRL) or using the relevant equations for the three new bulk ice schemes, listed in section 2.4. The CNTRL is performed with the NPv6.12 version of LMDZ. All results are shown for one year of statistics (simulations and observations).

When estimating  $D_{eff}$  directly from  $v_m$ , the latter should not be tuned anymore. Nevertheless, due to the coarse spatial resolution, we kept a scaling factor FALLICE of 0.9. A 3 times larger  $v_m$  than the one in the control simulation leads to a much smaller amount of high clouds, and therefore, we had to retune other parameters to meet the constraint of the radiative flux balance at the top of the atmosphere (TOA). The chosen values for EPMAX and RQH for these simulations are summarized in Table 1 (a).

To untangle the benefits gained by the retuning of these parameters from those gained by introducing the additional T dependence for  $v_m$ , we performed sensitivity simulations. In the first set of simulations, we

**Table 1**  
Tuning Parameters Relevant for UT Cloud Properties and TOA Fluxes in the CNTRL, (a) in the Simulations Using the New Bulk Ice Parameterizations and (b) in Those for Sensitivity Tests

	FALLICE	EPMAX	RQH
CNTRL	0.3	0.9985	0.40
(a) New parameterizations			
Empirical $v_m$ and $D_{eff}(v_m)$	0.9	0.9990	0.08
PSDM $v_m$ and $D_{eff}$	0.9	0.9988	0.11
PSDM $v_m$ and $D_{eff}(v_m)$	0.9	0.9988	0.11
(b) Sensitivity studies			
FALLICE+	0.5	0.9985	0.40
RQH-	0.3	0.9985	0.10
EPMAX+	0.3	0.9990	0.40
Scaled PSDM $v_m$	0.3	0.9985	0.40

changed each tuning parameter (FALLICE, RQH, EPMAX in Table 1 (b)) one at a time, but without imposing TOA radiation balance. In the last simulation (scaled PSDM  $v_m$  in Table 1 (b)), we scaled  $v_m$  of the PSDM parameterization to adjust it to the same average  $v_m$  as in the CNTRL. This means that  $v_m$  is again unrealistically small, but the TOA radiative fluxes are balanced, and  $v_m$  now depends on IWC and T instead of IWC only.

Before we analyze the effects on UT cloud and cloud system properties, we present in Figure 6 weighted joint T-IWC frequency of occurrence for all simulated ice clouds, over the entire globe, separately for the CNTRL and the three new bulk ice cloud scheme simulations. In comparison to Figure 7a of Delanoë et al. (2011), which presents weighted joint T-IWC frequency of occurrence obtained from CALIPSO-CloudSat retrievals, we observe a better agreement with the new bulk ice cloud scheme simulations than with the CNTRL: a larger population at warmer T and larger IWC and a less steep slope toward cold T and small IWC.

#### 4.2. Evaluation of Total UT Cloud Cover

Figure 7 presents zonal mean distributions of observed and simulated total UT cloud cover in boreal winter (December-January-February) and in boreal summer (June-July-August). Compared to the observations, the CNTRL shows a fractional UT cloud coverage about 0.08 smaller in the tropics and midlatitudes, while in the polar latitudes the values are similar (June-July-August) or even above (December-January-February) the ones of AIRS and IASI. As the AIRS/IASI simulator was applied to the simulation results, we compare in both cases clouds with  $\epsilon_{cld} > 0.1$ . This fixed  $\epsilon_{cld}$  threshold removes about 5 to 10% UT cloud amount (in the case that these thinner clouds appear alone or are accompanied by low-level clouds), compared to the CALIPSO-GOCCP data set (Chepfer et al., 2010). The latter uses active lidar observations and is generally used for the evaluation of cloud cover simulated by the LMDZ model. One also has to keep in mind that the performance of IR sounders in cloud detection over snow is slightly lower than the one of active instruments (Stubenrauch et al., 2017).

According to Figure 7 all three new bulk ice scheme simulations better agree with the observations in the tropics and midlatitudes, with a UT cloud cover increased by about 0.05. The PSDM parameterizations, with a slightly larger UT cloud cover in the midlatitudes, seem to improve the agreement with the data even more.

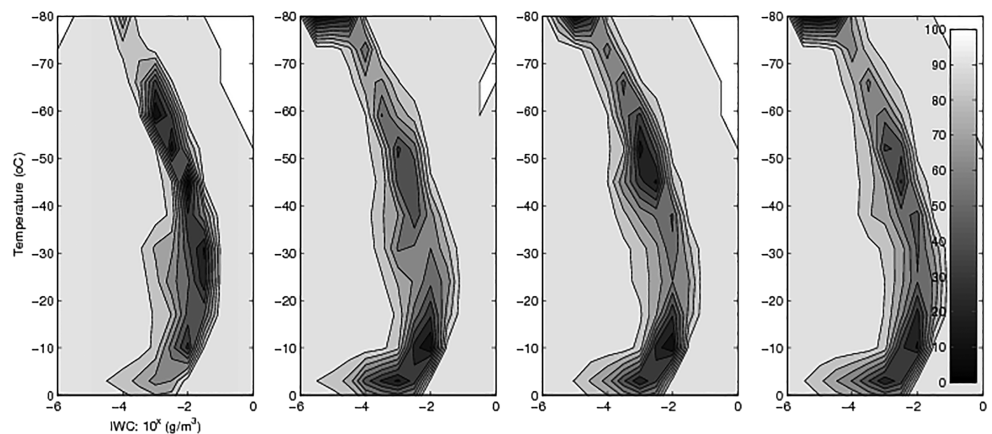


**Figure 6.** Weighted joint T-IWC frequency of occurrence for simulations of July of CNTRL and using the empirical  $v_m$  and  $D_{eff}(v_m)$ , PSDM  $v_m$  and  $D_{eff}(v_m)$ , and PSDM  $v_m$  and  $D_{eff}$  bulk ice schemes (from left to right), averaged over the globe. The new bulk ice schemes are in better agreement with the radar-lidar satellite observations presented in Delanoë et al. (2011, Figure 7a).



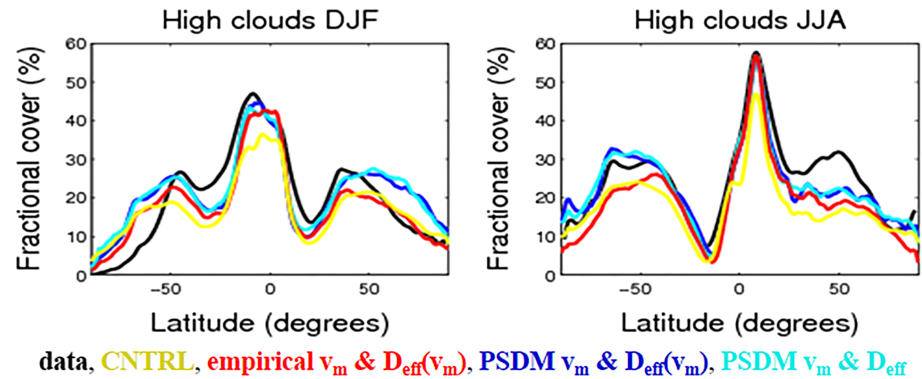


**Figure 7.** Zonal mean distributions of UT cloud amount from the new bulk ice schemes compared to AIRS and IASI observations and to the CNTRL, separately (eft) for boreal winter and (right) for boreal summer.

### 4.3. Evaluation of UT Cloud Types

One advantage of the AIRS/IASI cloud observation simulator is to provide the occurrence and the properties of high opaque (Cb), cirrus (Ci), and thin cirrus (thCi) within each grid cell. Figure 8 presents their zonal mean cover, with the sum of the three parts adding up to the total UT cloud cover. In the tropics, the CNTRL represents too much Cb and not enough thCi and Ci. This indicates that the too small UT cloud cover is partially compensated by a too large UT cloud emissivity to obtain a reasonable longwave cloud radiative effect. The increased UT cloud cover of the new bulk ice scheme simulations is linked to an increase in Ci and thCi, which strengthens the agreement with the data. The empirical parameterization produces slightly less Cb, in better agreement with the data, while the ratios between thCi and Ci as well as between tropical Cb and midlatitude Cb seem to be slightly more realistic when using the PSDM parameterizations. At this level we do not observe a mentionable difference between the two expressions for  $D_{eff}$ .

The improvements seen in the simulations using the new bulk ice cloud schemes can be due to the schemes themselves or due to the revised tuning parameters. Since increasing  $v_m$  to realistic values leads to a strong decrease of the UT cloud cover (Figure 8, second plot of bottom panel), the UT relative water subgrid variability, RQH, had to be strongly decreased and EPMAX had to be slightly increased. In the sensitivity simulations one further notices that introducing the T dependence of  $v_m$  but keeping the same tuning parameters as in the CNTRL (“scaled PSDM  $v_m$ ” simulation) already leads to a slightly better partitioning between Ci and thCi. An increase of EPMAX affects mostly the tropics and slightly improves the relative contributions of Cb, Ci, and thCi. A decrease in RQH increases the UT cloud cover everywhere and also improves the relative contributions of Cb, Ci, and thCi. Overall, both changes, the introduction of the T dependence of  $v_m$ , and the retuning necessary to reach realistic values of  $v_m$ , seem to be favorable for the UT cloud cover and emissivity.

### 4.4. Evaluation Using UT Cloud System Statistics

In a next step, we analyze the UT cloud system statistics. The UT cloud systems have been constructed as described in section 3.4.

According to the observations, 61% of all UT cloud systems are convective systems in the tropics, and 37% of all UT cloud systems are convective or frontal systems (including convective cores) in the midlatitudes. Their properties are displayed in Table 2, while the properties of the remaining UT cloud systems are shown in Table 3. The tropical systems are in general larger, colder, and less emissive than the systems in the midlatitudes (median values of  $223 \times 10^4 \text{ km}^2$ , 223 K, 0.67 compared to  $88 \times 10^4 \text{ km}^2$ , 232 K, 0.77, respectively). This is also true for all simulations. However, the coverage relative to the one of all UT cloud systems, T, and

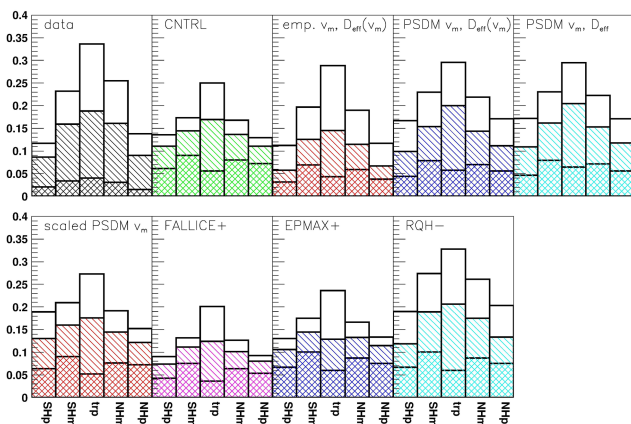


**Figure 8.** Zonal mean statistics of Cb (double hatched), Ci (hatched), and thCi (transparent) from observations, CNTRL, new bulk ice schemes, and sensitivity experiments. Latitude bands cover 90°S–60°S (SHp), 60°S–20°S (SHm), 20°S–20°N (trp), 20°N–60°N (NHm), and 60°N–90°N (NHp). Statistics includes boreal winter and summer.



**Table 2**

*Properties of Convective/Frontal Cloud Systems, in the Tropics (30°N–30°S, Top) and in the Midlatitudes (30°N–60°N and 30°S–60°S, Bottom): Median Values (Means in Parentheses)*

Tropics	Relative coverage (%)	System size ( $10^4$ km <sup>2</sup> )	$T$ (K)	$\epsilon$	Thin Ci/anvil subgrid Cb fraction	
Data	61	233 (473)	223 (224)	0.67 (0.65)	0.31 (0.29)	0.10
Control	52	66 (143)	213 (216)	0.79 (0.73)	0.20 (0.20)	0.44
Empirical $v_m$ and $D_e$ ( $v_m$ )	81	142 (446)	216 (221)	0.63 (0.61)	0.46 (0.42)	0.28
PSDM $v_m$ and $D_e$ ( $D_m$ )	85	91 (376)	214 (219)	0.71 (0.64)	0.27 (0.27)	0.35
PSDM $v_m$ and $D_e$ ( $v_m$ )	84	98 (427)	215 (220)	0.69 (0.64)	0.29 (0.29)	0.34
Midlatitudes	Relative coverage (%)	System size ( $10^4$ km <sup>2</sup> )	$T$ (K)	$\epsilon$	Thin Ci/anvil subgrid Cb fraction	
Data	37	88 (132)	232 (232)	0.77 (0.72)	0.14 (0.14)	0.15
Control	18	16 (28)	223 (224)	0.87 (0.65)	0.09 (0.15)	0.79
Empirical $v_m$ and $D_e$ ( $v_m$ )	22	38 (83)	226 (228)	0.76 (0.69)	0.35 (0.34)	0.57
PSDM $v_m$ and $D_e$ ( $D_m$ )	24	47 (108)	223 (225)	0.78 (0.70)	0.27 (0.27)	0.54
PSDM $v_m$ and $D_e$ ( $v_m$ )	24	47 (107)	223 (225)	0.77 (0.71)	0.31 (0.30)	0.55

*Note.* Convective cores are defined with average grid cell  $UT \epsilon_{\text{cld}} \geq 0.95$ , subgrid Cb fraction  $> 0.1$ , and rain rate  $> 0$ .

especially the system size of the CNTRL are smaller while the mean emissivity is larger than those of the observed cloud systems (median values of  $66 \times 10^4$  km<sup>2</sup>, 213 K, 0.79 in the tropics and  $16 \times 10^4$  km<sup>2</sup>, 223 K, 0.87 in the midlatitudes). The new bulk ice scheme simulations present a considerable increase of the first two variables and a decrease of the mean emissivity, leading to an improved agreement with the observations.

This is even more visible in the top panels of Figures 9 and 10, presenting the tropics and the midlatitudes, respectively. The distributions of cloud system size get broader, in better agreement with the observed distributions, especially in the midlatitudes. In the tropics, the distributions are now slightly broader than the observed one. The  $T$  distribution of the cloud systems of the CNTRL has a very narrow peak around 213 K, while the observed distribution has a very broad peak around 235 K. The new bulk ice scheme simulations keep a peak at about 213 K, but considerably broaden the distribution toward larger values, thus getting closer to the observations. In the midlatitudes, the  $T$  distribution of the CNTRL is broader, with a peak around 220 K, and the new bulk ice scheme simulations shift the distribution toward larger values, also in better agreement with the observations. Furthermore, these simulations show emissivity distributions broadened toward smaller values, leading especially in the tropics to systems with average emissivities smaller than 0.5, which are missing in the CNTRL but occurring in the observations. However, in the tropics they introduce a peak of cloud systems with an average emissivity close to 1.

This behavior can be understood by investigating the distributions of the sensitivity simulations in the bottom panels of Figures 9 and 10: The decrease of RQH has a strong influence, broadening the distributions and shifting  $T$  toward larger values, in closer agreement to the observations. The introduction of the

**Table 3**

*Properties of UT Cloud Systems With No Convective Cores, in the Tropics (30°N–30°S, Top) and in the Midlatitudes (30°N–60°N and 30°S–60°S, Bottom): Median Values (Means in Parentheses)*

Tropics	Relative coverage (%)	System size ( $10^4$ km <sup>2</sup> )	$T$ (K)	$\epsilon$	Thin Ci/system
Data	39	3 (14)	232 (230)	0.53 (0.52)	0.48 (0.51)
Control	48	6 (23)	212 (213)	0.67 (0.67)	0.33 (0.37)
Empirical $v_m$ and $D_e$ ( $v_m$ )	19	3 (15)	221 (223)	0.55 (0.58)	0.62 (0.56)
PSDM $v_m$ and $D_e$ ( $v_m$ )	16	3 (14)	220 (222)	0.63 (0.62)	0.46 (0.49)
PSDM $v_m$ and $D_e$ ( $D_m$ )	15	3 (13)	219 (221)	0.66 (0.64)	0.40 (0.45)
Midlatitudes	Relative coverage (%)	System size ( $10^4$ km <sup>2</sup> )	$T$ (K)	$\epsilon$	Thin Ci/system
Data	63	3 (16)	233 (232)	0.62 (0.60)	0.32 (0.39)
Control	82	6 (18)	219 (220)	0.92 (0.87)	0.15 (0.24)
Empirical $v_m$ and $D_e$ ( $v_m$ )	78	6 (22)	229 (230)	0.84 (0.78)	0.31 (0.38)
PSDM $v_m$ and $D_e$ ( $v_m$ )	76	6 (28)	226 (227)	0.84 (0.79)	0.30 (0.36)
PSDM $v_m$ and $D_e$ ( $D_m$ )	76	6 (30)	225 (226)	0.84 (0.79)	0.26 (0.33)

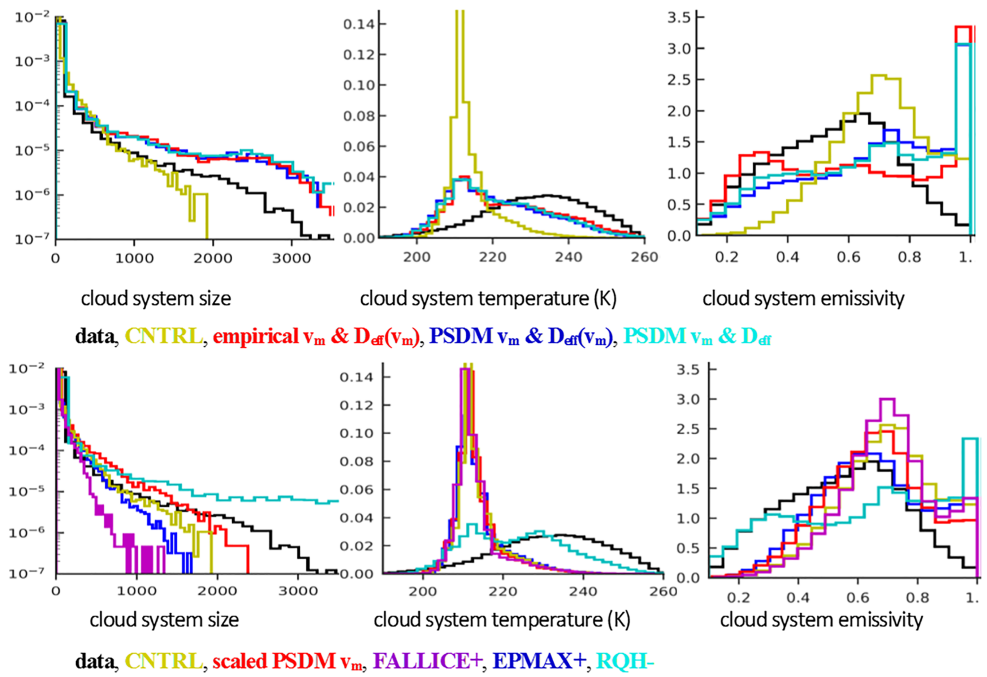


**Figure 9.** Normalized frequency distributions of (left) UT cloud system size, (middle) average cloud top T, and (right) emissivity in the tropics, comparing the (top) new bulk ice cloud schemes and (bottom) sensitivity experiments to the observations and the CNTRL. Data statistics combined from AIRS and IASI.

additional T dependence on  $v_m$  (scaled  $v_m$ ) leads also to a broadening of the cloud system size and emissivity distributions, especially in the midlatitudes. The effect is small, as  $v_m$  is kept small. Increasing  $v_m$  to a realistic value (by increasing FALLICE) leads to a much narrower cloud system size distribution, which can

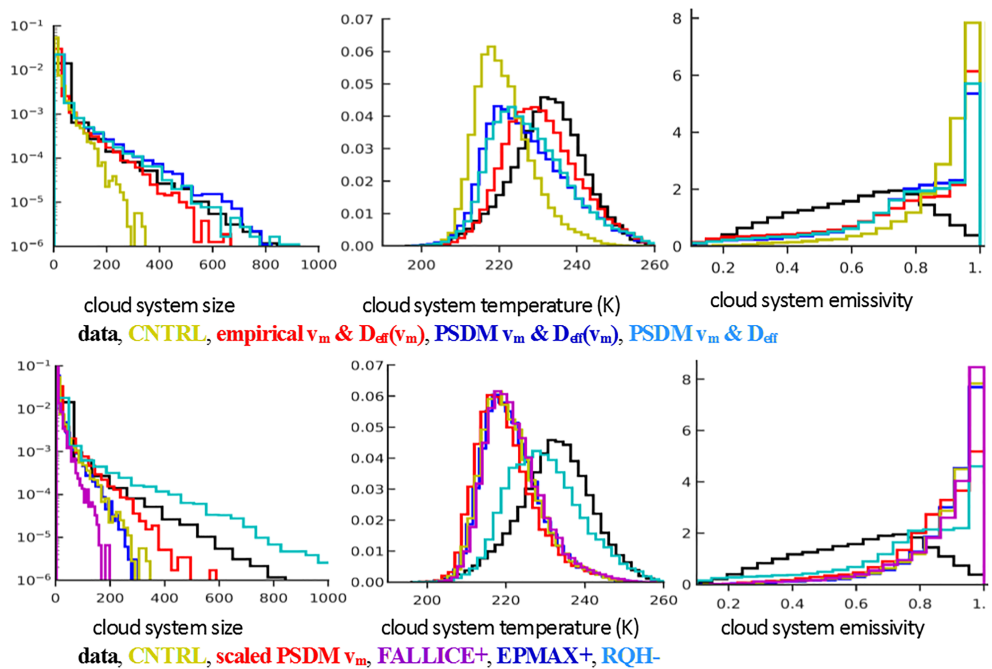


**Figure 10.** (left) Properties of Convective of UT cloud system size, (middle) average cloud top T, and (right) emissivity in the midlatitudes, comparing the (top) new bulk ice cloud schemes and (bottom) sensitivity experiments to the observations and the CNTRL. Data statistics combined from AIRS and IASI.

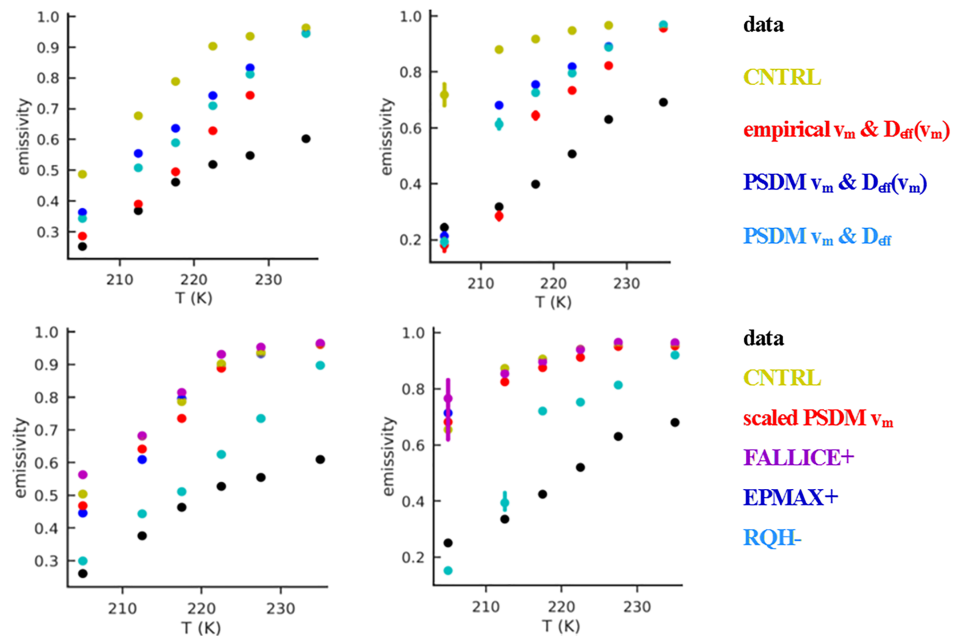


**Figure 11.** Median cloud system emissivity as function of cloud system temperature (left) in the tropics and (right) in the midlatitudes, comparing the (top) new bulk ice cloud schemes and (bottom) sensitivity experiments to the observations and to the CNTRL. Statistics includes all UT cloud systems, with data combined from AIRS and IASI.

then be compensated by decreasing RQH. In the tropics, one can also slightly increase EPMAX in order to reduce the cloud system emissivity, without introducing the peak close to 1.

It is interesting to note, that while all three bulk ice schemes lead to similar results in the tropics, the empirical parameterization leads to a T distribution slightly closer to the observations in the midlatitudes. It is difficult to decide from our simulations if this is directly linked to the parameterization or to the slightly different tuning parameters (slightly larger EPMAX and slightly smaller RQH than for the PSDM parameterizations), as both play a role in the results (Table 2 and Figures 9 and 10).

The last two columns of Table 2 present the fraction of thin cirrus within the anvils and the subgrid Cb fraction. Within the grid cells, the CNTRL produces more than 4 times as much Cb than observed (0.44 and 0.79, in the tropics and in the midlatitudes, respectively, compared to 0.10 and 0.15). The fact that the simulated UT clouds seem to be optically too thick is also reflected in the thin cirrus fraction within the anvils which is too small: 0.20 and 0.09, in the tropics and midlatitudes, respectively, compared to 0.31 and 0.14 from the observations. Nevertheless, both the CNTRL and the observations show a smaller fraction of subgrid Cb fraction and a larger thin cirrus over anvil ratio in the tropics compared to the midlatitudes. The new bulk ice scheme simulations lead in general to a better agreement with the observations by decreasing the subgrid Cb fraction to 0.28–0.35 in the tropics and to 0.54–0.57 in the midlatitudes and by increasing the thin cirrus over anvil ratio to 0.27–0.46 in the tropics and 0.27–0.35 in the midlatitudes. The latter seems now to be overestimated in the midlatitudes. This will be further investigated by analyzing Figure 11.

From Table 3 we deduce that UT cloud systems with no convective core have a small relative coverage in the tropics, while their relative coverage is more important in the midlatitudes (39% and 63% observed, 48% and 82% in the CNTRL, and 15%–19% and 76%–78% for the new bulk ice scheme simulations, respectively). The size of these UT cloud systems is much smaller than the one of the convective cloud systems displayed in Table 2. While the size of these systems is similar in the tropics and midlatitudes (median value of  $6 \times 10^4 \text{ km}^2$ ) in the CNTRL, the observations and the new bulk ice scheme simulations show a smaller size of these systems in the tropics (median value of  $3 \times 10^4 \text{ km}^2$ ) than in the midlatitudes (median value of  $6 \times 10^4 \text{ km}^2$ ). As for the convective systems, T and emissivity of these systems are also changed. The new bulk ice scheme simulations show larger average T and a smaller average emissivity of the systems, leading to a better agreement with the observations. From the sensitivity studies (Tables S1

and S2 in the supporting information) we conclude that the additional T dependence of  $v_m$  already helps to decrease the average emissivity and to increase the ratio of thin cirrus within the UT cloud systems, while the necessary retuning when introducing a larger, realistic fall speed, in particular via the decrease of RQH, leads to a more realistic T of the systems.

Figure 11 illustrates how the median T and emissivity of the UT cloud systems are related, separately in the tropics (left) and in the midlatitudes (right). The observations are compared to the CNTRL and to the new bulk scheme simulations in the top panel and to the sensitivity experiments in the bottom panel. In general, the median emissivity decreases with decreasing T, as the water vapor within the atmosphere also decreases with height. The observations reveal a smaller slope in the tropics than in the midlatitudes, because deep convection is able to inject water vapor from the lower troposphere into the upper troposphere (see also section 5). As the CNTRL produces clouds which are too opaque, the emissivity values are far above the ones from the data, and the decrease is stronger in the tropics than in the midlatitudes, in contrast to the data. The IR sounder observations might slightly underestimate the emissivity in the case of not completely cloud-filled footprints. This effect should however be much smaller than the difference with the CNTRL, as the global mean emissivity of ice clouds retrieved from AIRS lies well between the one from the MODIS-CERES (Minnis et al., 2011) and the PATMOS-x (Heidinger & Pavolonis, 2009) retrievals, which use instruments with a better spatial resolution (Stubenrauch et al., 2013).

The new bulk ice scheme simulations produce ice clouds with smaller emissivity, in particular at colder T: in the tropics the relationship between T and emissivity looks thus more similar to the one obtained from the data. In the midlatitudes, the new bulk ice scheme simulations also show a reduced emissivity, but around T = 215 K one observes a large step of 0.2 toward smaller emissivity. Considering the sensitivity experiments, this behavior is due to the reduction of RQH. This indicates that the parameterization of the UT relative water subgrid variability (section 3.1) has to be revised. One possibility would be to parameterize the height, at which it is set to a constant value RQH, as a function of tropopause height, since the depth of the troposphere decreases with latitude.

By investigating the simulated zonal relative humidity profiles (Figure S1), we observe that the zonal relative humidity profiles of the CNTRL are too dry in the upper troposphere, compared to ERA-Interim reanalyses (Dee et al., 2011). The new bulk ice scheme simulations lead to a slightly larger relative humidity in the upper troposphere, improving the agreement with the reanalyses, except at higher latitudes above 250 hPa, where it is now too humid. The effect is slightly stronger for the simulation including the empirical parameterization, as the RQH is slightly lower than for those using the PSDM parameterizations. This result agrees with the analysis of Figure 11, displaying the discontinuity in the emissivity decrease around 215 K.

In conclusion, this analysis has shown that the representation of the relative width of P(q) within the grid cells has to be revised. This will be done in a near future.

## 5. Process-Oriented Evaluation Using the Cloud System Concept

In this section we investigate the results of the different simulations in a more process-oriented way. First we analyze the tropical convective cloud system properties as a function of convective core fraction within the system. This variable is a good proxy of the cloud system life cycle stage (e.g., Machado et al., 1998), decreasing from 1 at formation to 0 at dissipation of the convective cloud system. This approach was applied on the CIRS AIRS cloud data by Protopapadaki et al. (2017), to reveal that during the life cycle the cloud system size increases while the rain rate and the anvil emissivity decrease. The convective core size first increases and then decreases during dissipation.

At the spatial resolution of the GCM simulations the data show a similar behavior, as shown in Figure 12. The convective core fraction within the cloud system is computed as the number of grid cells with UT clouds with an average grid cell emissivity  $>0.95$  divided by the number of grid cells belonging to the cloud system and weighted by the subgrid Cb fraction. Since the simulated subgrid Cb fraction is larger than the observed one (Table 3), we have multiplied their convective core fraction by a factor of 0.4 in order to compare similar statistics within the different convective core fraction intervals (Figure S2). Thus, the convective core fraction in Figure 12 only indicates qualitatively the life stage cycle: decreasing convective core fraction within the convective cloud system corresponds to increasing system age. Nevertheless, following the statistical

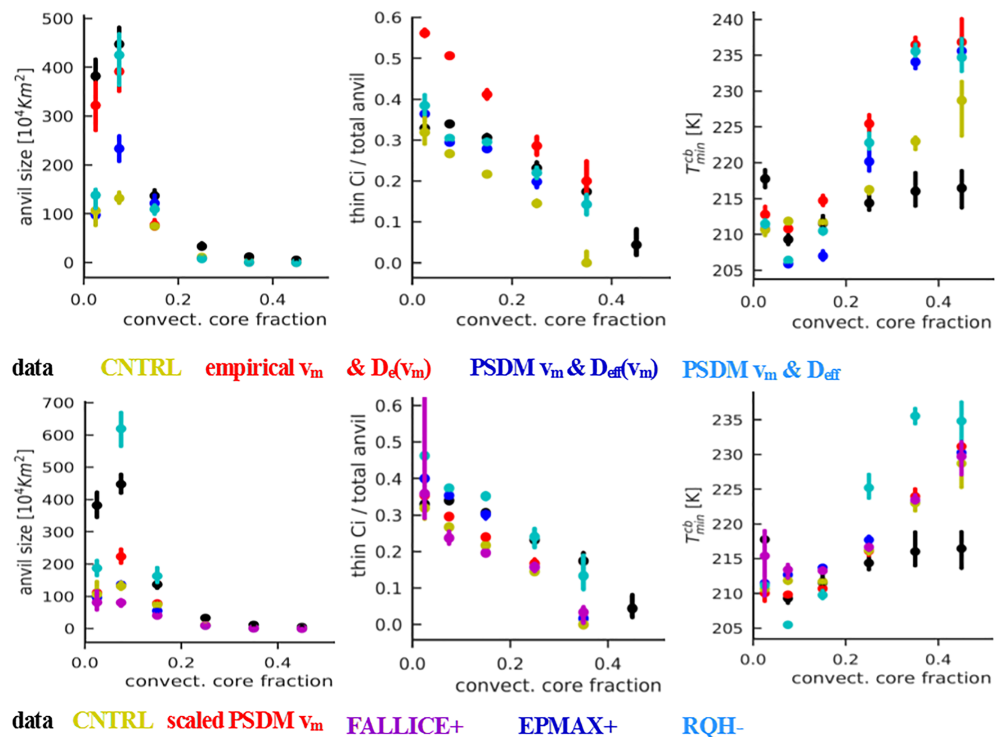


**Figure 12.** Anvil size, ratio of thin cirrus over total anvil size, and minimum T within convective core as function of system life cycle for tropical convective cloud systems, comparing the (top) new bulk ice cloud schemes and (bottom) sensitivity studies to the observations and the control run. Decreasing convective core fraction within the convective cloud system corresponds to increasing system age. Data from AIRS.

behavior of the convective cloud system properties along their life cycle gives an interesting opportunity for a deeper evaluation. The anvils of the LMDZ simulations are connected to the convection by EPMAX which provides the fraction left for detrainment and is at present very small. On the other side, UT relative humidity available for large-scale condensation originates from lower tropospheric humidity which is transported by convection into the upper troposphere via strong updrafts.

Figure 12 shows that the anvil size first increases during the life cycle. When dissipation occurs (convective core fraction nearly 0), it decreases. This is valid for the observations as well as for all simulations. However, the maximum anvil size produced by the CNTRL is 4 times less than the one obtained from the observations. The new bulk ice scheme simulations show in general an increased maximum cloud system size, in much better agreement with the data. The increase of the thin cirrus fraction within the anvil during the cloud system life cycle agrees quite well between the CNTRL and the observations. The fraction of thin cirrus within the anvil of the simulations including the PSDM parameterizations are in very good agreement with the data, while the one using the empirical parameterization increases more strongly, leading to too much thin cirrus in the second half of the life cycle. Considering the sensitivity experiments, the additional T dependence of  $v_m$  increases the agreement with the data, but as the  $v_m$  is scaled by 0.3, the effect is small. The largest change is again given by the decrease of RQH, increasing the maximum anvil size, while both the increase of EPMAX as well as the decrease of RQH lead to a slight increase in the slope of the thin cirrus fraction within the anvil. Therefore, the larger values in the thin cirrus fraction of the empirical parameterization may be produced by the slightly larger EPMAX and slightly smaller RQH compared to the ones of the PSDM parameterizations.

Since this article also intends to more generally introduce the UT cloud system approach as a process-oriented evaluation of parameterizations concerning convection and detrainment, Figure 13 presents anvil size and fraction of thin cirrus within the anvil as a function of minimum temperature within the convective cores,  $T_{\text{min}}^{\text{cb}}$ . The latter is a good proxy for convective depth (Protopapadaki et al., 2017): its decrease corresponds to an increase in convective depth. In general, convective cloud systems first develop in height and



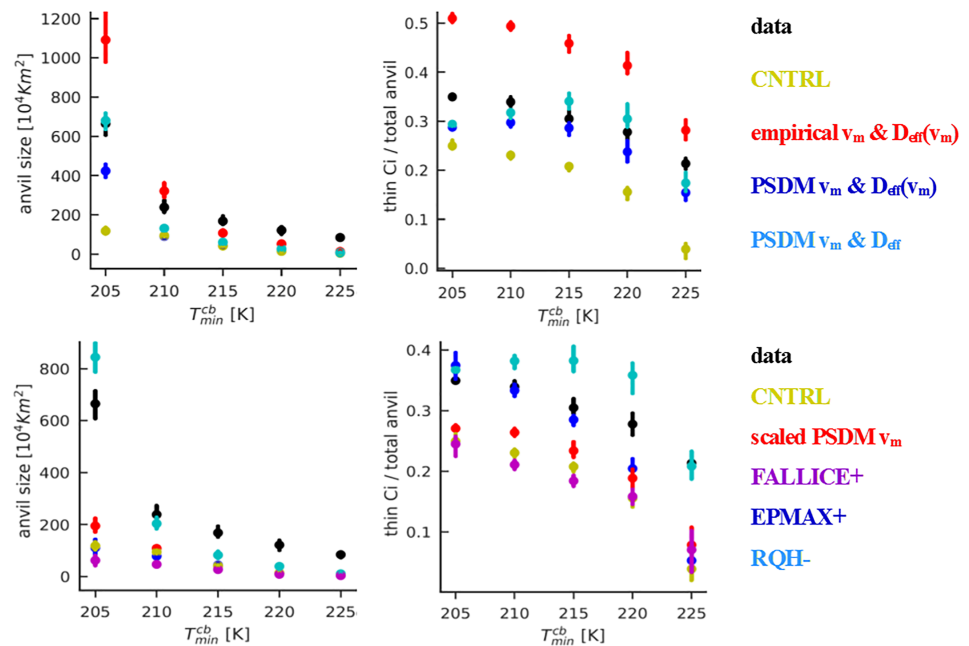


**Figure 13.** Anvil size and ratio of thin cirrus over total anvil size as function of convective depth for tropical mature convective cloud systems, comparing the (top) new bulk ice cloud schemes and (bottom) sensitivity studies to the observations and the CNTRL. A decreasing minimum top temperature within the convective cores corresponds to an increasing convective depth. Data from AIRS.

then in width. The height development is illustrated in Figure 12, with  $T_{\min}^{\text{Cb}}$  decreasing (or height increasing) along the cloud system life cycle. It is interesting to note that maximum height and maximum system size are reached closely before dissipation. Then the height seems to sink slightly ( $T_{\min}^{\text{Cb}}$  slightly increasing). A similar behavior is observed for all simulations and for the data, although the convective depth seems to increase stronger in the simulations.

In order to decouple the height increase during the development stage from the convective depth reached at maturity, we compare in Figure 13 only convective cloud systems in their “mature” stage. Because of the relatively coarse spatial resolution, this mature stage is only loosely defined: with a convective core fraction within the cloud systems between 0.05 and 0.30. While the data show a visible increase of anvil size with increasing convective depth, the anvil size from the CNTRL is nearly constant. The new bulk ice scheme simulations reproduce this increase, in much better agreement with the data. The sensitivity experiments show that the introduced T dependence as well as the decrease of RQH are responsible for this. The thin cirrus fraction within the anvil also increases with convective depth. This phenomenon can be explained by (1) environmental predisposition (larger relative humidity and temperature stratification at higher altitude) and (2) UT humidification originating from convection. At present, we do not yet know which effect is more important. Interestingly, all simulations show a similar effect, with the CNTRL lying below the data and the empirical parameterization above. The sensitivity experiments show that the additional T dependence of  $v_m$  increases the agreement. While an increase of EPMAX leads to a more realistic slope, a decrease of RQH increases the thin cirrus fraction already in the middle T range. Results including all convective systems, and not only the mature convective systems, are similar (Figure S3).

## 6. Conclusions and Outlook

This article presents a new approach to further constrain parameterizations which influence UT cloud properties. Hyperspectral sounder cloud data from AIRS and IASI and the analogous cloud observation simulator provide not only grid cell averages but also grid cell fractions of high opaque, cirrus and thin cirrus clouds and their properties. Furthermore, a novel cloud system concept is proposed for a more

process-oriented evaluation. Cloud systems are built from grid cells with clouds of similar height, and convective cores are determined from opaque, raining clouds. This allows us to study the horizontal extent and emissivity structure of the anvils and to relate them to the life stage and convective depth of the convective systems.

These new evaluation methods are used to investigate the impact of new bulk ice schemes on the climate simulations of the LMDZ model. The bulk ice scheme of the current version of the LMDZ model uses independent  $v_m$  and  $D_{\text{eff}}$  parameterizations, one depending on IWC and the other on T. Moreover,  $v_m$  is one of the tuning parameters to achieve TOA radiation balance, which at present leads to unrealistically small values, except for TTL cirrus, and is one reason why the simulated UT clouds are too cold.

We have constructed several schemes from published parameterizations obtained from large statistics of recent observations, paying attention to their validity range. All these new schemes have a realistic  $v_m$ , which depends on both IWC and T, and they coherently couple cloud physics (cloud life time influenced by  $v_m$ ) and cloud radiative effects (influenced by  $D_{\text{eff}}$ ). We compare three different schemes: one empirical scheme determining  $v_m$  as a function of IWC and T and then relates  $D_{\text{eff}}$  directly to  $v_m$ , and two schemes based on a PSD moment parameterization for  $v_m$ , with  $D_{\text{eff}}$  once determined from  $v_m$  as in the first scheme and once from the moments of the same PSDs as  $v_m$ .

Our analyses have shown that an additional T dependence of  $v_m$  improves the agreement with the observations, in particular when considering the UT cloud system size and subgrid fractions of thin cirrus and Cb. This improvement is already achieved even when  $v_m$  is still scaled by 0.3 to achieve radiation balance at TOA (in particular Figure 8 and Table S1).

The introduction of realistic values of  $v_m$  (changing the scaling factor FALLICE from 0.3 to 0.9) made it necessary to adjust two other tuning parameters, because the UT cloud amount strongly decreased. This was achieved by decreasing the relative width of the subgrid UT total water distribution, RQH, and by slightly increasing the maximum precipitation efficiency, EPMAX. Thus, the final climate simulations integrate the new bulk ice schemes as well as a relatively large adjustment of two parameters which had to be retuned for radiation balance at TOA. Therefore, we have also tested the sensitivity of the UT cloud and cloud system properties to these tuning parameters. An increase of EPMAX only affects the tropics, leading to a slightly decreased emissivity of cold convective cloud systems and increased thin cirrus fraction within the anvil, which agrees better with the data. A decrease in RQH strongly influences UT clouds, by increasing their amount and the thin cirrus fraction. The distributions of the size of the convective cloud systems and their temperature are also broadened, further improving the simulation results. A quite large change of RQH (from 0.4 to 0.1) was necessary to balance the effect of increasing FALLICE.

In general, the simulations including the more coherent bulk ice schemes and the new values of the tuning parameters agree better with the cloud data. This is particularly true when considering the new observational metrics such as the occurrence of different UT cloud types and the distributions of the UT cloud system properties. The current LMDZ simulations produce less UT clouds than observed, in particular in the tropics, while the clouds are too opaque and their temperature is too low. When considering UT cloud systems, these are too small. Integrating the new bulk ice schemes improves the partition of the UT cloud types by increasing cirrus and thin cirrus compared to Cb. The distributions of the UT cloud system properties, like their horizontal extent, T, and emissivity, also improve.

One outcome of the UT cloud system analysis, which revealed a high sensitivity to RQH, is that the formulation of the subgrid UT total water distribution width should be improved. In particular, the behavior of cloud system emissivity with temperature has shown that one may revise its dependence with altitude, in particular the altitude above which it is set constant. Although the database of water variability developed by Kahn and Teixeira (2009) from AIRS observations is based on water vapor and not on total water, it still may guide a new parameterization (Quaas, 2012). These data already indicate contrasts between land and sea and between inner tropics and subtropics.

All three new bulk ice schemes, with both  $v_m$  and  $D_{\text{eff}}$  depending on IWC and on T and with realistic values of  $v_m$ , improve the average quantities of the UT cloud systems as well as the process-oriented behavior of

convective cloud systems. However, as the adjustment of the tuning parameters also has a large effect, it is at present not possible to decide which of the three bulk ice schemes gives the best results. Connecting  $D_{\text{eff}}$  directly to  $v_m$  or deriving it from the same PSD moment parameterization as  $v_m$  provides very similar results. To test the  $D_{\text{eff}}$  parameterizations more in detail one needs radiative heating rates of the UT cloud systems.

While the empirical scheme mixes results from different observations, the PSDM parameterization uses the same PSDs to derive  $v_m$  and  $D_{\text{eff}}$ . A further advantage of the latter method is that we will be able to replace the  $D_{\text{eff}}$  concept by a parameterization of the ice crystal single scattering properties (SSP) directly as a function of IWC and T, using the same PSDs as for the PSDM  $v_m$  parameterization. Using directly the bulk extinction coefficient, single scattering albedo and asymmetry parameter for the radiative transfer computations allows to bypass  $D_{\text{eff}}$ . This method should be more precise, since the definition of  $D_{\text{eff}}$  is not generally applicable across the whole electromagnetic spectrum (e.g., Baran, 2012). This SSP parameterization is already implemented in the Met Office Unified Model (Baran et al., 2014, 2016), with the SSP fit parameters given for the spectral bands of the radiative transfer module of the Met Office Unified Model (B16).

In a next step we want to integrate the SSP parameterization into the LMDZ model which will provide then a completely coherent bulk ice scheme. Therefore, we will fit the SSPs as a function of IWC and T for the spectral bands of RRTM, using the database of B16.

For a detailed evaluation of the  $D_{\text{eff}}$  and SSP parameterizations, we will compare the radiative heating rates of the anvils of the convective cloud systems. For this we are currently laterally extending the radiative heating rates from CALIPSO and CloudSat (Henderson et al., 2013) across the UT cloud systems from AIRS (Hemmer et al., 2019).

These new evaluation methods, in particular the process-oriented cloud system analysis, are also valuable to evaluate other parameterizations, in particular those which influence convective strength and detrainment. The AIRS/IASI simulator will be made available in the Cloud feedback model intercomparison project Observation Simulator Package (COSP; Bodas-Salcedo et al., 2011).

#### Acknowledgments

The authors thank F. Hourdin, A. Baran, P. Field, G. Mace, and A. Heymsfield for the fruitful exchanges. The parameterizations presented are found in the cited references and have been summarized in the supporting information. The AIRS-CIRS and IASI-CIRS cloud climatologies will be distributed by the French Data Centre AERIS (<https://www.aeris-data.fr>). This study also benefited from the IPSL mesocenter ESPRI facility which is supported by CNRS, UPMC, Labex L-IPSL, CNES, and Ecole Polytechnique. In particular, the data and the LMDZ simulation outputs used for this research are available via anonymous ftp at [ftp://ftp.climserv.ipsl.polytechnique.fr/Data/4Papers/CloudSystemMetrics4GCM\\_Stubenrauch2019/](ftp://ftp.climserv.ipsl.polytechnique.fr/Data/4Papers/CloudSystemMetrics4GCM_Stubenrauch2019/). This work was supported by CNRS and by CNES and granted access to the HPC resources of IDRIS under allocation 0292 made by GENCI. The authors thank the members of the IASI and AIRS science teams for their efforts and cooperation in providing the data as well as the engineers and space agencies who control the data quality. In addition, we thank two anonymous referees and the Editor for their thoughtful comments, which very much improved the quality of the manuscript.

#### References

- Baran, A. J. (2012). From the single-scattering properties of ice crystals to climate prediction: A way forward. *Atmospheric Research*, *112*, 45–69. <https://doi.org/10.1016/j.atmosres.2012.04.010>
- Baran, A. J., Hill, P., Furtado, K., Field, P., & Manners, J. (2014). A coupled cloud physics–radiation parameterization of the bulk optical properties of cirrus and its impact on the Met Office Unified Model Global Atmosphere 5.0 configuration. *Journal of Climate*, *27*(20), 7725–7752. <https://doi.org/10.1175/JCLI-D-13-00700.1>
- Baran, A. J., Hill, P., Walters, D., Hardiman, S. C., Furtado, K., Field, P. R., & Manners, J. (2016). The impact of two coupled cirrus microphysics–radiation parameterizations on the temperature and specific humidity biases in the tropical tropopause layer in a climate model. *Journal of Climate*, *29*(14), 5299–5316. <https://doi.org/10.1175/JCLI-D-15-0821.1>
- Baran, A. J., & Labonnote, L.-C. (2007). A self-consistent scattering model for cirrus. 1: The solar region. *Quarterly Journal of the Royal Meteorological Society*, *133*(629), 1899–1912. <https://doi.org/10.1002/qj.164>
- Bodas-Salcedo, A., Webb, M. J., Bony, S., Chepfer, H., Dufresne, J.-L., Klein, S. A., et al. (2011). COSP: Satellite simulation software for model assessment. *Bulletin of the American Meteorological Society*, *92*, 1023–1043. <https://doi.org/10.1175/2011BAMS2856.1>
- Bony, S., & Emanuel, K. A. (2001). A parameterization of the cloudiness associated with cumulus convection: Evaluation using TOGA COARE data. *Journal of the Atmospheric Sciences*, *58*(21), 3158–3183. [https://doi.org/10.1175/1520-0469\(2001\)058<3158:APOTCA>2.0.CO;2](https://doi.org/10.1175/1520-0469(2001)058<3158:APOTCA>2.0.CO;2)
- Boucher, O., Randall, D., Artaxo, P., Bretherton, C., Feingold, G., Forster, P., et al. (2013). Clouds and aerosols. In T. F. Stocker, D. Qin, G.-K. Plattner, M. Tignor, S. K. Allen, J. Doschung, A. Nauels, Y. Xia, V. Bex, & P. M. Midgley (Eds.), *Climate Change 2013: The Physical Science Basis. Contribution of Working Group I to the Fifth Assessment Report of the Intergovernmental Panel on Climate Change* (pp. 571–657). Cambridge: Cambridge University Press. <https://doi.org/10.1017/CBO9781107415324.016>
- Chahine, M. T., Pagano, T. S., Aumann, H. H., Atlas, R., Barnett, C., Blaisdell, J., et al. (2006). AIRS: Improving weather forecasting and providing new data on greenhouse gases. *Bulletin of the American Meteorological Society*, *87*, 911–926. <https://doi.org/10.1175/BAMS-87-7-911>
- Chepfer, H., Bony, S., Winker, D., Cesana, G., Dufresne, J. L., Minnis, P., et al. (2010). The GCM Oriented Calipso Cloud Product (CALIPSO-GOCCP). *Journal of Geophysical Research*, *115*, D00H16. <https://doi.org/10.1029/2009JD012251>
- Dee, D. P., Uppala, S. M., Simmons, A. J., Berrisford, P., Poli, P., Kobayashi, S., et al. (2011). The ERA-Interim reanalysis: Configuration and performance of the data assimilation system. *Quarterly Journal of the Royal Meteorological Society*, *137*(656), 553–597. <https://doi.org/10.1002/qj.828>
- Delanoë, J., Hogan, R. J., Forbes, R. M., Bodas-Salcedo, A., & Stein, T. H. M. (2011). Evaluation of ice cloud representation in the ECMWF and UK Met Office models using CloudSat and CALIPSO data. *Quarterly Journal of the Royal Meteorological Society*, *137*(661), 2064–2078. <https://doi.org/10.1002/qj.882>
- Deng, M., & Mace, G. G. (2006). Cirrus microphysical properties and air motion statistics using cloud radar Doppler moments. Part I: Algorithm description. *Journal of Applied Meteorology and Climatology*, *45*(12), 1690–1709. <https://doi.org/10.1175/JAM2433.1>

- Deng, M., & Mace, G. G. (2008). Cirrus cloud microphysical properties and air motion statistics using cloud radar Doppler moments: Water content, particle size, and sedimentation relationships. *Geophysical Research Letters*, *35*, L17808. <https://doi.org/10.1029/2008GL035054>
- Ebert, E. E., & Curry, J. A. (1992). A parameterization of ice cloud optical properties for climate models. *Journal of Geophysical Research*, *97*(D4), 3831–3836. <https://doi.org/10.1029/91JD02472>
- Emanuel, K. A. (1993). The effect of convective response time on WISHE modes. *Journal of the Atmospheric Sciences*, *50*(12), 1763–1776. [https://doi.org/10.1175/1520-0469\(1993\)050<1763:TEOCRT>2.0.CO;2](https://doi.org/10.1175/1520-0469(1993)050<1763:TEOCRT>2.0.CO;2)
- Emanuel, K. A., & Živković-Rothman, M. (1999). Development and evaluation of a convection scheme for use in climate models. *Journal of the Atmospheric Sciences*, *56*(11), 1766–1782. [https://doi.org/10.1175/1520-0469\(1999\)056<1766:DAEOAC>2.0.CO;2](https://doi.org/10.1175/1520-0469(1999)056<1766:DAEOAC>2.0.CO;2)
- Eyring, V., Bony, S., Meehl, G. A., Senior, C. A., Stevens, B., Stouffer, R. J., & Taylor, K. E. (2016). Overview of the Coupled Model Intercomparison Project Phase 6 (CMIP6) experimental design and organization. *Geoscientific Model Development*, *9*(5), 1937–1958. <https://doi.org/10.5194/gmd-9-1937-2016>
- Ferrier, B. S. (1994). A double-moment multiple-phase four-class bulk ice scheme. Part I: Description. *Journal of the Atmospheric Sciences*, *51*, 249–280. [https://doi.org/10.1175/1520-0469\(1994\)051<0249:ADMMPF>2.0.CO;2](https://doi.org/10.1175/1520-0469(1994)051<0249:ADMMPF>2.0.CO;2)
- Field, P. R., Heymsfield, A. J., & Bansemer, A. (2007). Snow size distribution parameterization for midlatitude and tropical ice clouds. *Journal of the Atmospheric Sciences*, *64*(12), 4346–4365. <https://doi.org/10.1175/2007JAS2344.1>
- Fu, Q. (1996). An accurate parameterization of the solar radiative properties of cirrus clouds for climate models. *Journal of Climate*, *9*(9), 2058–2082. [https://doi.org/10.1175/1520-0442\(1996\)009<2058:AAPOTS>2.0.CO;2](https://doi.org/10.1175/1520-0442(1996)009<2058:AAPOTS>2.0.CO;2)
- Furtado, K., Field, P. R., Cotton, R., & Baran, A. J. (2015). The sensitivity of simulated high clouds to ice crystal fall speed, shape and size distribution. *Quarterly Journal of the Royal Meteorological Society*, *141*(690), 1546–1559. <https://doi.org/10.1002/qj.2457>
- Grandpeix, J.-Y., & Lafore, J.-P. (2010). A density current parameterization coupled with Emanuel's convection scheme. Part I: The models. *Journal of the Atmospheric Sciences*, *67*(4), 881–897. <https://doi.org/10.1175/2009JAS3044.1>
- Heidinger, A. K., & Pavolonis, M. J. (2009). Gazing at cirrus clouds for 25 years through a split window. Part I: Methodology. *Journal of Applied Meteorology and Climatology*, *48*(6), 1100–1116. <https://doi.org/10.1175/2008JAMC1882.1>
- Hemmer, F., Stubenrauch, C. J., & Protospadaki, S. E. (2019). Predicting 3D radiative heating rate fields from synergistic A-Train observations combined with deep learning techniques. *Proceed. of 9<sup>th</sup> Int. Workshop on Climate Informatics*, Paris, 2–4 Oct, 2019.
- Henderson, D. S., L'Ecuyer, T., Stephens, G., Partain, P., & Sekiguchi, M. (2013). A multisensor perspective on the radiative impacts of clouds and aerosols. *Journal of Applied Meteorology and Climatology*, *52*(4), 853–871. <https://doi.org/10.1175/JAMC-D-12-025.1>
- Hendricks, J., Falb, A., Stubenrauch, C. J., Lohmann, U., & Emde, C. (2010). A method for comparing properties of cirrus clouds in global climate models with those retrieved from IR sounder satellite observations. *Meteorologische Zeitschrift*, *19*(6), 577–589. <https://doi.org/10.1127/0941-2948/2010/0484>
- Heymsfield, A., Krämer, M., Wood, N. B., Gettelman, A., Field, P. R., & Liu, G. (2017). Dependence of the ice water content and snowfall rate on temperature, globally: Comparison of in situ observations, satellite active remote sensing retrievals, and global climate model simulations. *Journal of Applied Meteorology and Climatology*, *56*(1), 189–215. <https://doi.org/10.1175/JAMC-D-16-0230.1>
- Heymsfield, A. J. (2003). Properties of tropical and midlatitude ice cloud particle ensembles. Part II: Applications for mesoscale and climate models. *Journal of the Atmospheric Sciences*, *60*(21), 2592–2611. [https://doi.org/10.1175/1520-0469\(2003\)060<2592:POTAMI>2.0.CO;2](https://doi.org/10.1175/1520-0469(2003)060<2592:POTAMI>2.0.CO;2)
- Heymsfield, A. J., & Donner, L. J. (1990). A scheme for parameterizing ice-cloud water content in general circulation models. *Journal of the Atmospheric Sciences*, *47*(15), 1865–1877. [https://doi.org/10.1175/15200469\(1990\)047<1865:ASFPPC>2.0.CO;2](https://doi.org/10.1175/15200469(1990)047<1865:ASFPPC>2.0.CO;2)
- Heymsfield, A. J., & Platt, C. (1984). A parameterization of the particle size spectrum of ice clouds in terms of the ambient temperature and the ice water content. *Journal of the Atmospheric Sciences*, *41*(5), 846–855. [https://doi.org/10.1175/1520-0469\(1984\)041<0846:APOTPS>2.0.CO;2](https://doi.org/10.1175/1520-0469(1984)041<0846:APOTPS>2.0.CO;2)
- Heymsfield, A. J., Schmitt, C., & Bansemer, A. (2013). Ice cloud particle size distributions and pressure-dependent terminal velocities from in situ observations at temperatures from 0° to –86 °C. *Journal of the Atmospheric Sciences*, *70*(12), 4123–4154. <https://doi.org/10.1175/JAS-D-12-0124.1>
- Hilton, F., Armante, R., August, T., Barnet, C., Bouchard, A., Camy-Peyret, C., et al. (2012). Hyperspectral Earth observation from IASI. *Bulletin of the American Meteorological Society*, *93*(3), 347–370. <https://doi.org/10.1175/BAMS-D-11-00027.1>
- Hourdin, F., Grandpeix, J.-Y., Rio, C., Bony, S., Jam, A., Cheruy, F., et al. (2013). LMDZ5B: The atmospheric component of the IPSL climate model with revisited parameterizations for clouds and convection. *Climate Dynamics*, *40*(9–10), 2193–2222. <https://doi.org/10.1007/s00382-012-1343-y>
- Hourdin, F., Mauritsen, T., Gettelman, A., Golaz, J., Balaji, V., Duan, Q., et al. (2017). The art and science of climate model tuning. *Bulletin of the American Meteorological Society*, *98*(3), 589–602. <https://doi.org/10.1175/BAMS-D-15-00135.1>
- Kahn, B. H., & Teixeira, J. (2009). A global climatology of temperature and water vapor variance scaling from the Atmospheric Infrared Sounder. *Journal of Climate*, *22*(20), 5558–5576. <https://doi.org/10.1175/2009JCLI2934.1>
- Kummerow, C., Ferraro, R., & Randel, D. (2015). *AMSRE/Aqua L2B Global Swath Surface Precipitation GSFC Profiling Algorithm, version 3*. Boulder, Colorado USA: NASA National Snow and Ice Data Center Distributed Active Archive Center. [https://doi.org/10.5067/AMSRE/AE\\_RAIN.003](https://doi.org/10.5067/AMSRE/AE_RAIN.003)
- Liu, C., Zipser, E. J., & Nesbitt, S. W. (2007). Global distribution of tropical deep convection: Different perspectives from TRMM infrared and radar data. *Journal of Climate*, *20*(3), 489–503. <https://doi.org/10.1175/JCLI4023.1>
- Machado, L. A. T., Rossow, W. B., Guedes, R. L., & Walker, A. W. (1998). Life cycle variations of mesoscale convective systems over the Americas. *Monthly Weather Review*, *126*(6), 1630–1654. [https://doi.org/10.1175/1520-0493\(1998\)126<1630:LCVOMC>2.0.CO;2](https://doi.org/10.1175/1520-0493(1998)126<1630:LCVOMC>2.0.CO;2)
- Minnis, P., Sun-Mack, S., Young, D. F., Heck, P. W., Garber, D. P., Chen, Y., et al. (2011). CERES Edition-2 cloud property retrievals using TRMM VIRS and Terra and Aqua MODIS data, Part I: Algorithms. *IEEE Transactions on Geoscience and Remote Sensing*, *49*(11), 4374–4400. <https://doi.org/10.1109/TGRS.2011.2144601>
- Mitchell, D. L. (1996). Use of mass- and area-dimensional power laws for determining precipitation particle terminal velocities. *Journal of the Atmospheric Sciences*, *53*(12), 1710–1723. [https://doi.org/10.1175/1520-0469\(1996\)053<1710:UOMAAD>2.0.CO;2](https://doi.org/10.1175/1520-0469(1996)053<1710:UOMAAD>2.0.CO;2)
- Mitchell, D. L., Mishra, S., & Lawson, R. P. (2011). Representing the ice fall speed in climate models: Results from Tropical Composition, Cloud and Climate Coupling (TC4) and the Indirect and Semi-Direct Aerosol Campaign (ISDAC). *Journal of Geophysical Research*, *116*, D00T03. <https://doi.org/10.1029/2010JD015433>
- Morcrette, J.-J., Barker, H. W., Cole, J. N. S., Iacono, M. J., & Pincus, R. (2008). Impact of a new radiation package, McRad, in the ECMWF Integrated Forecast System. *Monthly Weather Review*, *136*(12), 4773–4798. <https://doi.org/10.1175/2008MWR2363.1>



- Protopapadaki, E.-S., Stubenrauch, C. J., & Feofilov, A. G. (2017). Upper tropospheric cloud systems derived from IR Sounders: Properties of cirrus anvils in the tropics. *Atmospheric Chemistry and Physics*, *17*(6), 3845–3859. <https://doi.org/10.5194/acp-17-3845-2017>
- Quaas, J. (2012). Evaluating the “critical relative humidity” as a measure of subgrid-scale variability of humidity in general circulation model cloud cover parameterizations using satellite data. *Journal of Geophysical Research*, *117*, D09208. <https://doi.org/10.1029/2012JD017495>
- Rio, C., Grandpeix, J. Y., Hourdin, F., Guichard, F., Couvreux, F., Lafore, J.-P., et al. (2013). Control of deep convection by sub-cloud lifting processes: The ALP closure in the LMDZ5B general circulation model. *Climate Dynamics*, *40*(9–10), 2271–2292. <https://doi.org/10.1007/s00382-012-1506-x>
- Roca, R., Aublanc, J., Chambon, P., Fiolleau, T., & Viltard, N. (2014). Robust observational quantification of the contribution of mesoscale convective systems to rainfall in the tropics. *Journal of Climate*, *27*(13), 4952–4958. <https://doi.org/10.1175/JCLI-D-13-00628.1>
- Sanderson, B. M., Piani, C., Ingram, W. J., Stone, D. A., & Allen, M. R. (2008). Towards constraining climate sensitivity by linear analysis of feedback patterns in thousands of perturbed-physics GCM simulations. *Climate Dynamics*, *30*(2–3), 175–190. <https://doi.org/10.1007/s00382-007-0280-7>
- Schmitt, C. G., & Heymsfield, A. J. (2009). The size distribution and mass weighted terminal velocity of low-latitude tropopause cirrus crystal populations. *Journal of the Atmospheric Sciences*, *66*(7), 2013–2028. <https://doi.org/10.1175/2009JAS3004.1>
- Stubenrauch, C. J., Chédin, A., Armante, R., & Scott, N. A. (1999). Clouds as seen by satellite sounders (3I) and imagers (ISCCP). Part II: A new approach for cloud parameter determination in the 3I algorithms. *Journal of Climate*, *12*(8), 2214–2223. [https://doi.org/10.1175/1520-0442\(1999\)012<2214:CASBSS>2.0.CO;2](https://doi.org/10.1175/1520-0442(1999)012<2214:CASBSS>2.0.CO;2)
- Stubenrauch, C. J., Cros, S., Guignard, A., & Lamquin, N. (2010). A six-year global cloud climatology from the Atmospheric InfraRed Sounder aboard the Aqua Satellite: Statistical analysis in synergy with CALIPSO and CloudSat. *Atmospheric Chemistry and Physics*, *10*, 7197–7214. <https://doi.org/10.5194/acp-10-7197-2010>
- Stubenrauch, C. J., Del Genio, A. D., & Rossow, W. B. (1997). Implementation of sub-grid cloud vertical structure inside a GCM and its effect on the radiation budget. *Journal of Climate*, *10*(2), 273–287. [https://doi.org/10.1175/1520-0442\(1997\)010<0273:IOSCVS>2.0.CO;2](https://doi.org/10.1175/1520-0442(1997)010<0273:IOSCVS>2.0.CO;2)
- Stubenrauch, C. J., Feofilov, A. G., Protopapadaki, E.-S., & Armante, R. (2017). Cloud climatologies from the InfraRed Sounders AIRS and IASI: Strengths and applications. *Atmospheric Chemistry and Physics*, *17*, 13,625–13,644. <https://doi.org/10.5194/acp-17-13625-2017>
- Stubenrauch, C. J., Rossow, W. B., Kinne, S., Ackerman, S., Cesana, G., Chepfer, H., et al. (2013). Assessment of global cloud datasets from satellites: Project and database initiated by the GEWEX radiation panel. *Bulletin of the American Meteorological Society*, *94*, 1031–1049. <https://doi.org/10.1175/BAMS-D-12-00117.1>
- Suzuki, T., Tanaka, M., & Nakajima, T. (1993). The microphysical feedback of cirrus cloud in climate-change. *Journal of The Meteorological Society of Japan*, *71*(6), 701–714. [https://doi.org/10.2151/jmsj1965.71.6\\_701](https://doi.org/10.2151/jmsj1965.71.6_701)
- Yuan, J., & Houze, R. A. Jr. (2010). Global variability of mesoscale convective system anvil structure from A-Train satellite data. *Journal of Climate*, *23*, 5864–5888. <https://doi.org/10.1175/2010JCLI3671.1>
- Zelinka, M. D., Zhou, C., & Klein, S. A. (2016). Insights from a refined decomposition of cloud feedbacks. *Geophysical Research Letters*, *43*, 9259–9269. <https://doi.org/10.1002/2016GL069917>

## References From the Supporting Information

- Cotton, R. J., Field, P. R., Ulanowski, Z., Kaye, P. H., Hirst, E., Greenaway, R. S., et al. (2013). The effective density of small ice particles obtained from in situ aircraft observations of mid-latitude cirrus. *Quarterly Journal of the Royal Meteorological Society*, *139*, 1923–1934. <https://doi.org/10.1002/qj.2058>
- Delanoë, J., Protat, A., Testud, J., Bouniol, D., Heymsfield, A. J., Bansemmer, A., et al. (2005). Statistical properties of the normalized ice particle size distribution. *Journal of Geophysical Research*, *110*, D10201. <https://doi.org/10.1029/2004JD005405>
- Erfani, E., & Mitchell, D. L. (2016). Developing and bounding ice particle mass- and area-dimension expressions for use in atmospheric models and remote sensing. *Atmospheric Chemistry and Physics*, *16*(7), 4379–4400. <https://doi.org/10.5194/acp-16-4379-2016>
- Locatelli, J. D., & Hobbs, P. V. (1974). Fall speeds and masses of solid precipitation particles. *Journal of Geophysical Research*, *79*(15), 2185–2197. <https://doi.org/10.1029/JC079i015p02185>
- Mitchell, D. L. (2002). Effective diameter in radiative transfer: General definition, applications, and limitations. *Journal of the Atmospheric Sciences*, *59*(15), 2330–2346. [https://doi.org/10.1175/1520-0469\(2002\)059<2330:EDIRTG>2.0.CO;2](https://doi.org/10.1175/1520-0469(2002)059<2330:EDIRTG>2.0.CO;2)
- Westbrook, C. D., Hogan, R. J., Illingworth, A. J., & O'Connor, E. J. (2007). Theory and observations of ice particle evolution in cirrus using Doppler radar: Evidence for aggregation. *Geophysical Research Letters*, *34*, L02824. <https://doi.org/10.1029/2006GL027863>